

**DIRECT COMPARISONS OF POLARIMETRIC C-BAND AND  
S-BAND MOMENTS IN SNOW**

BRANDON M. TAYLOR

A THESIS SUBMITTED TO THE FACULTY OF GRADUATE STUDIES  
IN PARTIAL FULFILMENT OF THE REQUIREMENTS  
FOR THE DEGREE OF

MASTER OF SCIENCE

GRADUATE PROGRAM IN EARTH AND SPACE SCIENCE  
YORK UNIVERSITY  
TORONTO, ONTARIO  
APRIL 2018

**DIRECT COMPARISONS OF  
POLARIMETRIC C-BAND AND S-BAND  
MOMENTS IN SNOW**

by **Brandon M. Taylor**

a thesis submitted to the Faculty of Graduate Studies of  
York University in partial fulfilment of the requirements  
for the degree of

**MASTER OF SCIENCE**  
© 2018

Permission has been granted to: a) YORK UNIVERSITY LIBRARIES to lend or sell copies of this dissertation in paper, microform or electronic formats, and b) LIBRARY AND ARCHIVES CANADA to reproduce, lend, distribute, or sell copies of this thesis anywhere in the world in microform, paper or electronic formats *and* to authorise or procure the reproduction, loan, distribution or sale of copies of this thesis anywhere in the world in microform, paper or electronic formats.

The author reserves other publication rights, and neither the thesis nor extensive extracts for it may be printed or otherwise reproduced without the author's written permission.

**DIRECT COMPARISONS OF POLARIMETRIC C-BAND AND  
S-BAND MOMENTS IN SNOW**

by **Brandon M. Taylor**

By virtue of submitting this document electronically, the author certifies that this is a true electronic equivalent of the copy of the thesis approved by York University for the award of the degree. No alteration of the content has occurred and if there are any minor variations in formatting, they are as a result of the conversion to Adobe Acrobat format (or similar software application).

Examination Committee Members:

1. George Isaac
2. Dave Sills
3. Peter Taylor
4. Fourth Examiner
5. Fifth Examiner
6. Sixth Examiner

## Abstract

Calibrating weather radars is an ongoing issue, and as radar networks age and requirements change, new methods will continue to be developed to address these issues. When the United States WSR-88D NEXRAD weather radar network was upgraded to dual-polarimetric capabilities from 2011-2013, there was a flurry of effort to handle the calibration requirements of the new equipment. Techniques for the estimating bias of differential reflectivity ( $Z_{DR}$ ) using external targets were developed to verify that the internal calibration procedures performed as expected. With the calibration of one radar known, it can be compared with another to verify the others performance. In this case, the National Weather Service Buffalo, NY WSR-88D is compared with its neighbor to the north, Environment Canada's King City radar. Comparisons are performed during two different subsets of precipitation events, those being synoptic and lake-effect snow events. The data are analyzed onto a common grid using a distance-weighting scheme, with a hydrometeor classification scheme used to filter for dry snow. It is shown that the agreement between the radars in terms of reflectivity is within the bounds of the canonical 1 dB bias threshold. Furthermore, while the previous external target method relies on the self-consistency principle and is only able to detect a negative bias, this method brings in an independent set of observations to diagnose both positive and negative biases.

# Table of Contents

<b>Abstract</b>	<b>iv</b>
<b>Table of Contents</b>	<b>v</b>
<b>List of Figures</b>	<b>vii</b>
<b>1 Chapter One</b>	<b>1</b>
1.1 Introduction . . . . .	1
1.2 Background . . . . .	2
1.2.1 Reflectivity Factor ( $Z_h$ ) . . . . .	2
1.2.2 Differential Reflectivity ( $Z_{dr}$ ) . . . . .	2
<b>2 Chapter Two</b>	<b>4</b>
2.1 Methodology . . . . .	4
2.1.1 Comparison of Radar Systems . . . . .	4
2.1.2 Distance-Weighting Scheme . . . . .	5
2.2 Selection of Cases . . . . .	8
2.3 Filtering Conditions . . . . .	9
2.3.1 Time Filter . . . . .	9
2.3.2 Gate Filters . . . . .	9
2.4 Advanced Statistical Techniques . . . . .	9
2.4.1 Kernel Density Estimation . . . . .	9
2.4.2 Orthonormal Linear Regression . . . . .	10
2.5 $Z_{DR}$ Bias Estimation . . . . .	11

<b>3 Chapter Three</b>	<b>12</b>
3.1 Event Comparisons . . . . .	12
3.1.1 18 January 2014 - Synoptic . . . . .	12
3.1.2 23 January 2014 - Lake-Effect . . . . .	15
3.1.3 1 February 2014 - Synoptic . . . . .	15
3.1.4 6 January 2015 - Lake-Effect . . . . .	17
3.1.5 7 January 2015 - Synoptic . . . . .	17
3.1.6 6 February 2015 - Synoptic . . . . .	17
3.1.7 14 February 2015 - Lake-Effect . . . . .	17
3.1.8 18 February 2015 - Lake-Effect . . . . .	17
3.1.9 10 February 2016 - Lake-Effect . . . . .	18
3.1.10 15 December 2016 - Synoptic . . . . .	18
3.1.11 $Z_{eH}$ Subset Direct Comparisons . . . . .	18
3.1.12 $Z_{DR}$ Subset Direct Comparison . . . . .	19
3.2 Initial Results . . . . .	19
<b>A Appendix A</b>	<b>41</b>
A.1 Upper-Air Charts . . . . .	41
A.2 Skew-T Charts . . . . .	41
A.3 Sounding Climatology . . . . .	41
<b>Bibliography</b>	<b>63</b>

## List of Figures

1.1	The location of the NWS Buffalo Radar (KBUF) and King City Radar (CWKR) are shown as red dots, with a 75 km range ring around each.	3
2.1	Bounding box of the study area, denoted by the green shading. (latitude, longitude) given for each corners. . . . .	4
2.2	Base moment comparisons between radars over Lake Ontario, with dimensions of 20x12.5 km. Left panels are in native radars coordinates, with gates outlined in black. Right panels are transformed to a common Cartesian grid, with grid cells outlined in black. . . . .	7
2.3	Illustration of the construction of 2D kernel density estimates. (Left) data points with individual kernels as grey dashed lines, (right) summed kernels = kernel density estimate. . . . .	10
2.4	Demonstration of an Orthonormal Linear Regression . . . . .	11
3.1	Gridded $Z_{eH}$ comparison for 18 January 2014. Time-average of all admitted scans. . . . .	13
3.2	Gridded $Z_{DR}$ comparison for 18 January 2014. Time-average of all admitted scans. . . . .	13
3.3	Direct comparisons for 18 January 2014. Dataset includes all admitted grid cells. . . . .	14
3.4	Histograms of $Z_{DR}$ (left), $Z_{DR}$ bias at CWKR, determined by subtracting the gridded, bias adjusted $Z_{DR}$ at KBUF from the $Z_{DR}$ at CWKR. Both datasets exclude matched points with KDE < 2. . . . .	14

3.5	Gridded $Z_{DR}$ comparison for 23 January 2014. Time-average of all admitted scans.	16
3.6	Direct comparisons for 23 January 2014. Dataset includes all admitted grid cells.	16
3.7	Histograms of $Z_{DR}$ (left), $Z_{DR}$ bias at CWKR, determined by subtracting the gridded, bias adjusted $Z_{DR}$ at KBUF from the $Z_{DR}$ at CWKR. Both datasets exclude matched points with KDE < 2.	20
3.8	Gridded $Z_{eH}$ comparison for 23 January 2014. Time-average of all admitted scans.	20
3.9	Gridded $Z_{eH}$ comparison for 1 February 2014. Time-average of all admitted scans.	21
3.10	Gridded $Z_{DR}$ comparison for 1 February 2014. Time-average of all admitted scans.	21
3.11	Direct comparisons for 1 February 2014. Dataset includes all admitted grid cells.	22
3.12	Histograms of $Z_{DR}$ (left), $Z_{DR}$ bias at CWKR, determined by subtracting the gridded, bias adjusted $Z_{DR}$ at KBUF from the $Z_{DR}$ at CWKR. Both datasets exclude matched points with KDE < 2.	22
3.13	Gridded $Z_{eH}$ comparison for 6 January 2015. Time-average of all admitted scans.	23
3.14	Gridded $Z_{DR}$ comparison for 6 January 2015. Time-average of all admitted scans.	23
3.15	Direct comparisons for 6 January 2015. Dataset includes all admitted grid cells.	24
3.16	Histograms of $Z_{DR}$ (left), $Z_{DR}$ bias at CWKR, determined by subtracting the gridded, bias adjusted $Z_{DR}$ at KBUF from the $Z_{DR}$ at CWKR. Both datasets exclude matched points with KDE < 2.	24
3.17	Gridded $Z_{eH}$ comparison for 7 January 2015. Time-average of all admitted scans.	25

3.18 Gridded $Z_{DR}$ comparison for 7 January 2015. Time-average of all admitted scans. . . . .	25
3.19 Direct comparisons for 7 January 2015. Dataset includes all admitted grid cells. . . . .	26
3.20 Histograms of $Z_{DR}$ (left), $Z_{DR}$ bias at CWKR, determined by subtracting the gridded, bias adjusted $Z_{DR}$ at KBUF from the $Z_{DR}$ at CWKR. Both datasets exclude matched points with KDE < 2. . . . .	26
3.21 Gridded $Z_{eH}$ comparison for 6 February 2015. Time-average of all admitted scans. . . . .	27
3.22 Gridded $Z_{DR}$ comparison for 6 February 2015. Time-average of all admitted scans. . . . .	27
3.23 Direct comparisons for 6 February 2015. Dataset includes all admitted grid cells. . . . .	28
3.24 Histograms of $Z_{DR}$ (left), $Z_{DR}$ bias at CWKR, determined by subtracting the gridded, bias adjusted $Z_{DR}$ at KBUF from the $Z_{DR}$ at CWKR. Both datasets exclude matched points with KDE < 2. . . . .	28
3.25 Gridded $Z_{eH}$ comparison for 14 February 2015. Time-average of all admitted scans. . . . .	29
3.26 Gridded $Z_{DR}$ comparison for 14 February 2015. Time-average of all admitted scans. . . . .	29
3.27 Direct comparisons for 14 February 2015. Dataset includes all admitted grid cells. . . . .	30
3.28 Histograms of $Z_{DR}$ (left), $Z_{DR}$ bias at CWKR, determined by subtracting the gridded, bias adjusted $Z_{DR}$ at KBUF from the $Z_{DR}$ at CWKR. Both datasets exclude matched points with KDE < 2. . . . .	30
3.29 Gridded $Z_{eH}$ comparison for 18 February 2015. Time-average of all admitted scans. . . . .	31
3.30 Gridded $Z_{DR}$ comparison for 18 February 2015. Time-average of all admitted scans. . . . .	31

3.31 Direct comparisons for 18 February 2015. Dataset includes all admitted grid cells. . . . .	32
3.32 Histograms of $Z_{DR}$ (left), $Z_{DR}$ bias at CWKR, determined by subtracting the gridded, bias adjusted $Z_{DR}$ at KBUF from the $Z_{DR}$ at CWKR. Both datasets exclude matched points with KDE < 2. . . . .	32
3.33 Gridded $Z_{eH}$ comparison for 10 February 2016. Time-average of all admitted scans. . . . .	33
3.34 Gridded $Z_{DR}$ comparison for 10 February 2016. Time-average of all admitted scans. . . . .	33
3.35 Direct comparisons for 10 February 2016. Dataset includes all admitted grid cells. . . . .	34
3.36 Histograms of $Z_{DR}$ (left), $Z_{DR}$ bias at CWKR, determined by subtracting the gridded, bias adjusted $Z_{DR}$ at KBUF from the $Z_{DR}$ at CWKR. Both datasets exclude matched points with KDE < 2. . . . .	34
3.37 Gridded $Z_{eH}$ comparison for 15 December 2016. Time-average of all admitted scans. . . . .	35
3.38 Gridded $Z_{DR}$ comparison for 15 December 2016. Time-average of all admitted scans. . . . .	35
3.39 Direct comparisons for 15 December 2016. Dataset includes all admitted grid cells. . . . .	36
3.40 Histograms of $Z_{DR}$ (left), $Z_{DR}$ bias at CWKR, determined by subtracting the gridded, bias adjusted $Z_{DR}$ at KBUF from the $Z_{DR}$ at CWKR. Both datasets exclude matched points with KDE < 2. . . . .	36
3.41 Scatter-plots of CWKR versus KBUF grid analyzed reflectivity, with Kernel Density Estimation shading. The red line is an Orthonormal Linear Regression, with a black identity line. . . . .	37
3.42 Time averaged subsets of grid $Z_{eH}$ for KBUF and CWKR, with differences between the radars for each subset shown in the bottom panel.	38

3.43 Scatter-plots of CWKR versus KBUF grid analyzed differential reflectivity, with Kernel Density Estimation shading. The red line is an Orthonormal Linear Regression, with a black identity line. . . . .	39
3.44 Graphs of KBUF January-March 2014 $Z_{DR}$ bias estimates from NEXRAD rain (top panel) and snow (bottom panel) methods. Shading is a seven-day running median and points are daily median values. Tolerance levels are shaded light blue from $\pm 0.2$ dB. It is shown here that KBUF is outside of calibration tolerances. Data collected from archived NEXRAD Level III data. . . . .	40
A.1 500mb Geopotential Height at 06Z 18 January 2014. . . . .	42
A.2 500mb Geopotential Height at 06Z 23 January 2014 . . . . .	43
A.3 500mb Geopotential Height at 18Z 1 February 2014. . . . .	44
A.4 500mb Geopotential Height at 15Z 6 January 2015. . . . .	45
A.5 500mb Geopotential Height at 09Z 7 January 2015. . . . .	46
A.6 500mb Geopotential Height at 09Z 6 February 2015. . . . .	47
A.7 500mb Geopotential Height at 12Z 14 February 2015. . . . .	48
A.8 500mb Geopotential Height at 21Z 18 February 2015. . . . .	49
A.9 500mb Geopotential Height at 18Z 10 February 2016. . . . .	50
A.10 500mb Geopotential Height at 09Z 15 December 2016. . . . .	51
A.11 SkewT/Log-P Chart from the BUF Radiosonde launched at 12Z 18 January 2014 . . . . .	52
A.12 SkewT/Log-P Chart from the BUF Radiosonde launched at 00Z 23 January 2014 . . . . .	53
A.13 SkewT/Log-P Chart from the BUF Radiosonde launched at 12Z 1 February 2014 . . . . .	54
A.14 SkewT/Log-P Chart from the BUF Radiosonde launched at 00Z 6 January 2015 . . . . .	55
A.15 SkewT/Log-P Chart from the BUF Radiosonde launched at 12Z 7 January 2015 . . . . .	56

A.16 SkewT/Log-P Chart from the BUF Radiosonde launched at 00Z 6 February 2015 . . . . .	57
A.17 SkewT/Log-P Chart from the BUF Radiosonde launched at 12Z 14 February 2015 . . . . .	58
A.18 SkewT/Log-P Chart from the BUF Radiosonde launched at 00Z 18 February 2015 . . . . .	59
A.19 SkewT/Log-P Chart from the BUF Radiosonde launched at 12Z 10 February 2016 . . . . .	60
A.20 SkewT/Log-P Chart from the BUF Radiosonde launched at 12Z 15 December 2016 . . . . .	61
A.21 Sounding Precipitable Water Climatology for BUF . . . . .	62

# 1 Chapter One

## 1.1 Introduction

Weather radar is an invaluable tool for hydrometeorological purposes; with the refinement of operational polarimetric radars, it has become indispensable for quantitative precipitation estimation (QPE). Numerous studies have shown the skill of dual-pol estimators over traditional reflectivity-based algorithms, especially for rainfall cases. One approach is using polarimetric moments directly in empirically derived power law relations. Previously, two relations were developed by Hassan et al. (2017) ; one using just horizontal reflectivity ( $Z_H$ ), while the other incorporated differential reflectivity ( $Z_{DR}$ ) from the polarimetric C-Band radar at King City (CWKR). These algorithms were correlated with ground measurements of snowfall accumulation. The conclusion from the previous dataset is that the addition of  $Z_{DR}$  did not significantly improve the SWE estimates, but both still performed better than the legacy algorithm used by Environment Canada. Another approach for improving QPE estimates through polarimetric data is the classification of hydrometeor types, then using a corresponding relation matched to that type. While quantitative precipitation estimates contain statistical measurement error propagated from  $Z$  and  $Z_{DR}$ , this error is reduceable through spatial and temporal smoothing. Meanwhile, smoothing will not remove biases in the moments. This error will be propagated into QPE estimates, which is why its important to remove them. Here, it is shown that with biased  $Z_{DR}$  is used as input into Colorado State University hydrometeor classification scheme, it is sucessful at filtering for similiar dry snow targets in synoptic snowfall events with temperatures within the plate growth region, while failing in lake-effect snow events. The purpose

of the filtering is to yield better estimates of systematic bias.

## 1.2 Background

First, it is important to provide some background on the weather radar moments that are presented in this study, from both single and dual polarized signals. The convention for representing these moments symbolically hereafter is lower-case subscript for linear units and upper-case subscript for logarithmic units, i.e.  $Z_{DR}$  is logarithmic while  $Z_{dr}$  is linear.

### 1.2.1 Reflectivity Factor ( $Z_h$ )

$$Z_h = \int_0^\infty N(D)D^6dD \text{ (mm}^6/\text{m}^3\text{)} \quad (1.1)$$

The foremost moment derived from radar is the reflectivity factor ( $Z_h$ ), where the subscript denotes its derivation from the horizontally polarized signal. This variable measures the number density  $N(D)$  of hydrometeors of diameter  $D$  per unit volume, as presented in Equation 1.1. Due to uncertainties about what type of target is actually doing the scattering, it is typically represented as the equivalent reflectivity factor  $Z_{eh}$ , where  $Z_h = Z_{eh}$  if the targets are made of liquid water and are comparatively small to the wavelength (Fabry 2015). The two names are essentially interchangeable, but the nomenclature  $Z_{eh}$  will be used in this study to acknowledge the presence of non-ideal targets, e.g. snow crystals.

### 1.2.2 Differential Reflectivity ( $Z_{dr}$ )

Radar equipped with dual-polarimetric (dual-pol) capabilities are still an emerging technology, in terms of operational meteorological applications. These types of radar systems are capable of transmitting and receiving two orthogonally polarized electromagnetic waves in order to deduce more information about the microphysical structure of hydrometeors. One of the main variables this allows them to produce is  $Z_{DR}$ , defined as the ratio of the horizontal channel reflectivity ( $Z_H$ ) to the vertical

channel reflectivity  $Z_V$ ). This can be simplified to the difference between the two using the logarithmic quotient rule, since they are represented in logarithmic units. Equation 1.2 demonstrates this concept.

$$Z_{dr} = 10 * \log_{10}\left(\frac{Z_H}{Z_V}\right) = Z_h - Z_h \quad (1.2)$$

Although dual-pol radar has matured within the research community, operational deployment has been a much slower process. Many studies have been undertaken in regards to quantitative precipitation estimation using dual-pol variables for rainfall, but studies involving the estimation of snowfall liquid equivalent has been much more limited. In Canada, there is one active C-band weather radar with dual-pol capabilities. It is located north of Toronto, in King City, with rest of the network is currently undergoing an upgrade to polarimetric S-Band. Its neighbor to the south, KBUF, was upgraded to dual-pol in 2012 as part of a network wide upgrade. Figure

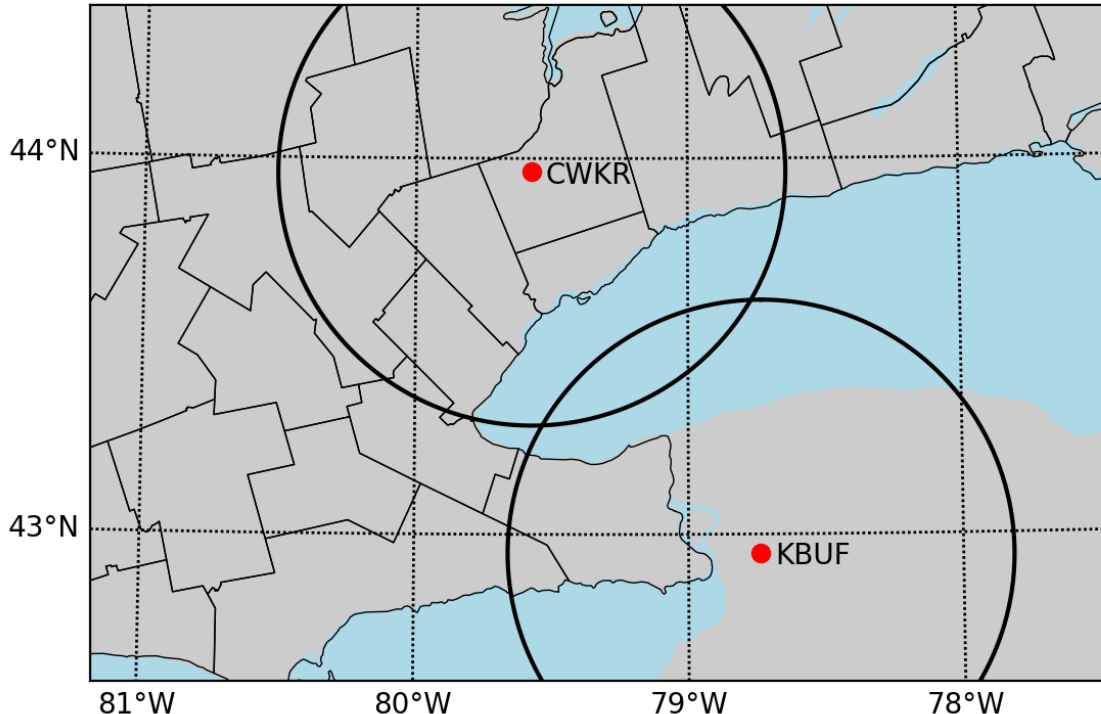


Figure 1.1: The location of the NWS Buffalo Radar (KBUF) and King City Radar (CWKR) are shown as red dots, with a 75 km range ring around each.

1.1 shows the geographic location of the radar sites in comparison with each other.

## 2 Chapter Two

### 2.1 Methodology

#### 2.1.1 Comparison of Radar Systems

Comparing two radar datasets is fraught with challenges; solutions to meet this challenge are presented herein. Even though the radar system characteristics are not identical, the measurements are comparable due to the design of the weather radar equation, which accounts for the sensitivity of the radar system itself (Rogers and Yau 1989). The area of study was chosen to ensure that the coinciding radar scans had similar resolution samples and beam heights. Lake Ontario happens to be the

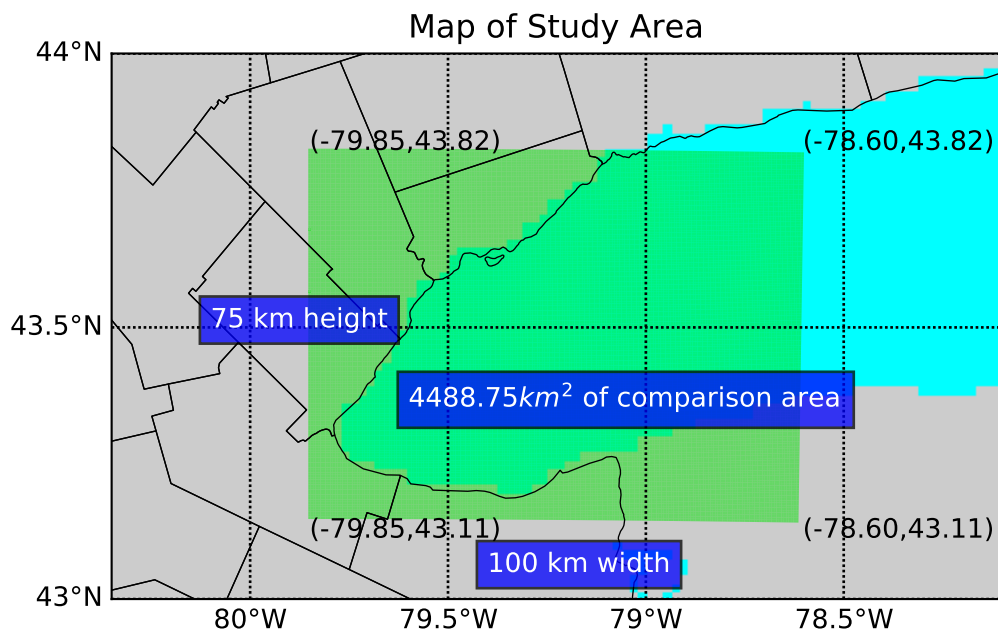


Figure 2.1: Bounding box of the study area, denoted by the green shading. (latitude, longitude) given for each corners.

perfect area to bound between the radars, therefore only data from areas over water inside the bounding box depicted in Figure 2.1 are used. This also ensures that no ground clutter is incorporated into the analyses.

### 2.1.1.1 Comparing Radar Characteristics

$$\bar{P}_r = \frac{\pi^3 c}{1024 \ln(2)} \left[ \frac{P_t \tau G^2 \theta^2}{\lambda^2} \right]_{dBZ_0} \left[ |K^2| \frac{Z_{eH}}{r^2} \right]_{TARGET} \quad (2.1)$$

As presented in Equation 2.1, the weather radar equation is defined by constant parameters dependent on the radar system characteristics, and varying properties related to the target. The target properties are dielectric constant ( $K$ ), range ( $r$ ) and equivalent reflectivity factor  $Z_{eH}$ . Conversely, the radar parameters ideally remain unchanged from their values upon installation of the radar system. These parameters form the radar constant, symbolically expressed as  $dBZ_0$ . The parameters that define this constant include the power transmitted ( $P_t$ ), the pulse length ( $\tau$ ), the antenna gain ( $G$ ), the angular beamwidth ( $\theta$ ), and the wavelength ( $\lambda$ ).

$$10 \log Z = 10 \log \bar{P}_r + 20 \log r - dBZ_0 \quad (2.2)$$

Equation 2.2 shows how  $dBZ_0$  is subtracted out from the full calculation of  $Z$ . Table 2.1 compares these parameters for both radar systems. The biggest difference between the two is the wavelength, with CWKR operating in the C frequency band and KBUF operating in the S frequency band. It should be noted that although KBUF has a larger physical beamwidth than CWKR, it achieves an effective azimuthal resolution of  $0.5^\circ$  through an over-sampled data windowing technique (Torres and Curtis 2007). Therefore, the two radars are matched in azimuthal resolution, while CWKR has twice the range resolution of KBUF.

### 2.1.2 Distance-Weighting Scheme

The biggest challenge when comparing radar resolution volumes measured by radars that are not co-located is resolving the differences in coordinate system. A resolution volume is defined as volume irradiated by the idealized Gaussian beam pattern for

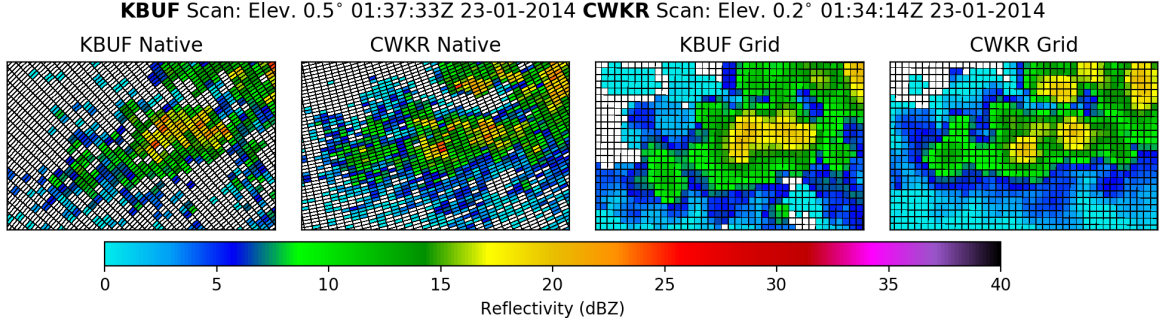
Table 2.1: Specifications of each radars system, with symbols as used in Eq. 2.2

field [symbol](unit)	King City (CWKR)	Buffalo (KBUF)
Wavelength [ $\lambda$ ](cm)	5 (C-Band)	10 (S-Band)
Beamwidth [ $\theta$ ] ( $^{\circ}$ )	0.62	0.92
Antenna Gain [G] (dB)	45.5	49.2
Transmitter Peak Power (kW)	250	1000
Pulse Length [ $\tau$ ] ( $\mu s$ )	0.8/2.0	1.5/4.5
Matched Elevation Angle ( $^{\circ}$ )	0.2	0.5
Range Resolution [ $r$ ] (m)	125	250

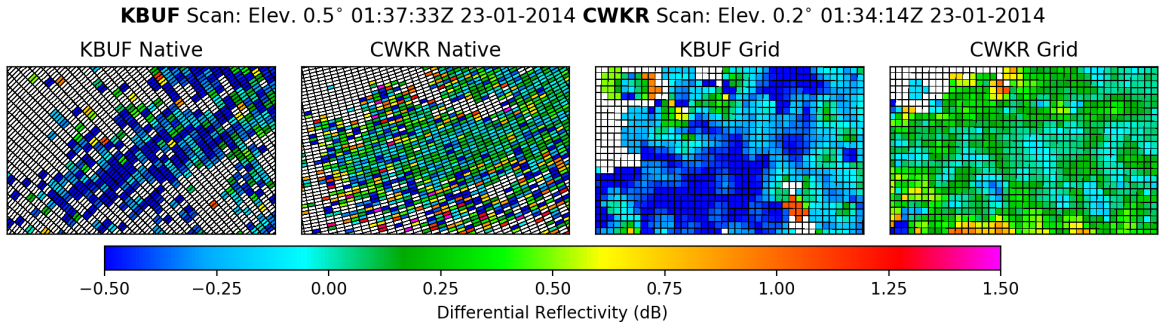
each range gate, otherwise known as a bin. Resolution volumes are sampled natively in the spherical coordinate system; although there may be some overlap, the shape of the bins will vary drastically. Differences between KBUF and CWKR bin geometry can be ascertained from Figure 2.2. These differences require the radar data to be objectively analyzed onto a common coordinate system, which can be achieved through a distance-weighting scheme. , which essentially convolves radar data with a distance-weighted function. This method was adopted in a more recent open source software module called the Python ARM Radar Toolkit (Py-ART) (Helmus and Collis 2016), which is used here. In accordance with the recommendations of Pauley and Wu (1990), a grid resolution ( $\Delta x$ ,  $\Delta y$ ) of 500 meters is chosen. A Barnes distance-weighting scheme is used for this analysis.

$$F_{i,j} = \sum_0^n F(b) * e^{-(d/ROI)^2} \quad (2.3)$$

The Gaussian weighting function used in said scheme is given in Equation 2.3. It shows that for some field  $F$ , the value of  $F$  in the Cartesian grid is determined by performing a summation over  $n$  number of bins  $b$  that are within the radius of influence (ROI) of the center point of the grid cell, and  $d$  is the horizontal distance from the native bin to the center point of the cell. Vertical distance is neglected, as only the



(a)  $Z_H$  comparison, shows the smooth transformation from an isotropic input to an isotropic gridded output.



(b)  $Z_{DR}$  comparison, in contrast with (a), shows the limitations of representing an anisotropic field with an isotropic distance-weighting function.

Figure 2.2: Base moment comparisons between radars over Lake Ontario, with dimensions of 20x12.5 km. Left panels are in native radars coordinates, with gates outlined in black. Right panels are transformed to a common Cartesian grid, with grid cells outlined in black.

lowest elevation angle from the radars are included for comparison.

$$ROI = D * \tan \theta \quad (2.4)$$

The definition of ROI is found in Equation 2.4, where  $D$  is the horizontal distance from the grid cell to the radar and  $\theta$  is the angular beamwidth. This completes the framework for comparing the radar datasets in this study.

Table 2.2: Critical level temperatures from radiosonde launched closest in time to the selected lake-effect snow events.

KBUF - Radiosonde	Radar Times	850mb T ( $^{\circ}C$ )	Lowest-Level T ( $^{\circ}C$ )
2014-01-23 00Z	0100-1000Z	-22.5	-14.9
2015-01-06 12Z	1200-1700Z	-20.1	-11.7
2015-02-14 12Z	1000-1400Z	-14.9	-6.9
2015-02-18 12Z	2100-2359Z	-17.3	-10.1
2016-02-10 12Z	1300-2359Z	-10.5	-2.7

Table 2.3: Critical level temperatures from radiosonde launched closest in time to the selected synoptic snow events.

KBUF - Radiosonde	Radar Times	850mb T ( $^{\circ}C$ )	Lowest-Level T ( $^{\circ}C$ )
2014-01-18 12Z	0600-0800Z	-11.3	-6.5
2015-01-07 12Z	0900-1100Z	-20.1	-11.7
2015-02-06 12Z	0900-1030Z	-16.3	-10.7
2016-01-06 12Z	0700-0900Z	-7.5	-0.7
2016-12-15 12Z	0920-1020Z	-20.3	-12.3

## 2.2 Selection of Cases

Cases selected for this study were chosen entirely based on the pattern of motion and banding of the radar echoes. Radar mosaics for the study area were manually examined, beginning in 2014. When time intervals with echoes in the study area were observed, it was noted whether they trained over the same area, or were progressive. The former are classified as lake-effect driven events, while the latter are synoptically driven events. Also, a tabulation of critical level temperatures for the five lake-effect snow events selected is shown in Table 2.2, while the synoptic events are shown in

Table 2.3. This shows ensures that all events were sufficiently below freezing, and dry snow was the predominant hydrometeor type.

## 2.3 Filtering Conditions

Several conditions were used to narrow down the selected sets to the best suited scans and individual gates for admission into the distance-weighting scheme.

### 2.3.1 Time Filter

Scan start times are compared between the radars, and if they are within four minutes of each other, the pair is admitted. For CWKR, there is a regular volume update frequency of ten minutes, while KBUF is variable based on the Volume Coverage Pattern (VCP) selected by the operator. The update frequency could be as short as every two minutes if the operator has activated Supplemental Adapative Intra-Volume Low-Level Scans (SAILS) mode.

### 2.3.2 Gate Filters

## 2.4 Advanced Statistical Techniques

Scatter plots directly comparing grid cells produced by the distance-weighting scheme are used in this study. This section discusses how advanced statistical techniques were leveraged to derive the most information from these plots.

### 2.4.1 Kernel Density Estimation

Large radar datasets contain an immense amount of data; this requires the distillation of data to the greatest statistical significance. Scatter-plots containing on the order of  $10^5$  points become visually overwhelming. To solve this problem, a Kernel Density Estimation (KDE) technique is used. A 2-D KDE is essentially a way to estimate the joint probability density function of two random variables (Silverman 1986). Figure

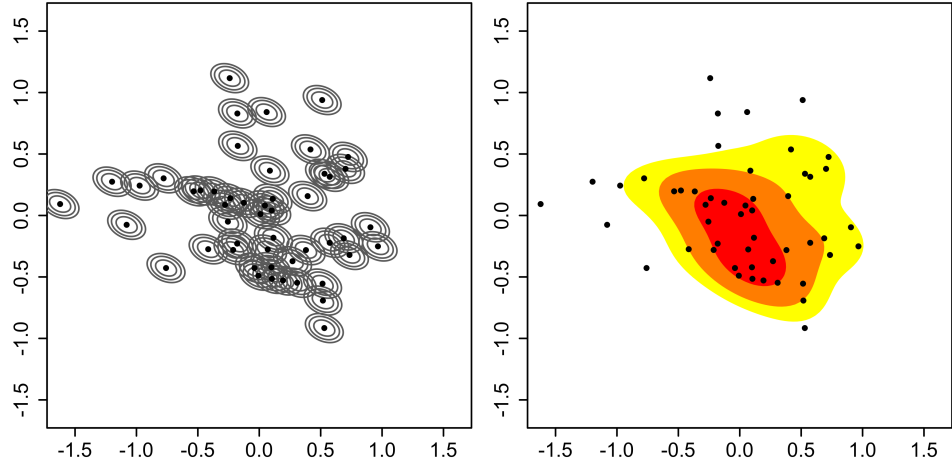


Figure 2.3: Illustration of the construction of 2D kernel density estimates. (Left) data points with individual kernels as grey dashed lines, (right) summed kernels = kernel density estimate.

2.3 demonstrates how this is achieved graphically, by first solving each individual kernel, then performing a summation. The units of the KDE can be thought of as a likelihood ratio. Furthermore, the units are normalized by the factor in Equation 2.5, where  $\mathbf{K}$  and  $\mathbf{C}$  are vectors representing measurements made at KBUF and CWKR respectively,  $n$  is the number of points, and  $R$  is the data resolution.

$$norm = n * R^2 * \sqrt{\text{Det}[2\pi * \text{Cov}[\mathbf{K}, \mathbf{C}] * n^{-1/6}]} \quad (2.5)$$

#### 2.4.2 Orthonormal Linear Regression

A hallmark of this study is the lack of ground truth. The sample sets compared,  $\mathbf{K}$  and  $\mathbf{C}$ , contain error prone, independent variables. Typically, scatter-plots compare an independent variable to a dependent variable. Instead of performing a standard linear regression between the variables, an orthonormal linear regression is used. This type of regression allows for error in both variables, by performing the least squares regression perpendicular to the initial fit instead of vertically (Markovsky and Huffel 2007). Figure 2.4 demonstrates this concept.

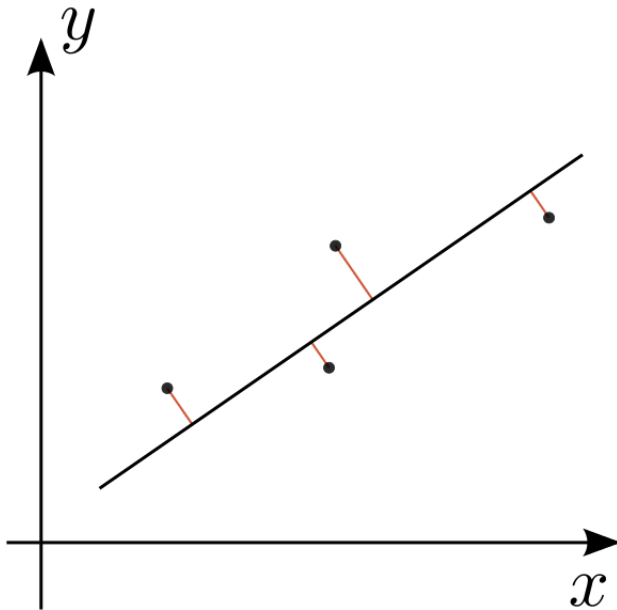


Figure 2.4: Demonstration of an Orthonormal Linear Regression

## 2.5 $Z_{DR}$ Bias Estimation

Although it is not possible to check absolute calibration of  $Z_{eH}$  when comparing two radars, it is possible to verify  $Z_{DR}$  calibration due to relative nature of the quantity (Zrnic et al. 2006). While radars are regularly calibrated using internal calibration procedures, an external check is useful for monitoring the time-varying component of calibration. The typical process for calibration of  $Z_{DR}$  is pointing the antenna to zenith and performing “bird bath” scans during light rain events (Hubbert and Pratte 2006). The  $Z_{DR}$  in light rain is expected to be 0 dB, therefore any offset from this is considered a bias; The signal processor subtracts out this bias to achieve the final output. Due to mechanical constraints, NEXRAD radars are unable to perform this procedure, but CWKR is (citation needed). NEXRAD radars disseminate a product which contains an estimate of  $Z_{DR}$  bias using the intrinsic properties of dry snow Zittel et al. (2015). The daily published offset will be used to adjust  $Z_{DR}$  values obtained from KBUF to diagnose any bias at CWKR.

## 3 Chapter Three

### 3.1 Event Comparisons

Now, we consider each of the selected events individually, demonstrating that the events were classified correctly, and breaking down the results from each case. Although it is nearly impossible to extricate lake influence from synoptically classified events, synoptic-scale ascent is considered the characterizing factor. Descriptions of the synoptic pattern during each event are given without reference; For reference, see Appendix A for the 500mb Geopotential Heights, Skew-T charts, and Sounding Climatology utilized. These descriptions are ancillary to the study and are provided to demonstrate a variety of patterns are represented.

#### 3.1.1 18 January 2014 - Synoptic

In this event, a weak shortwave is approaching Southern Ontario as it rounds the base of a longwave trough centered over the Eastern seaboard of the US. Ample synoptic scale lift and a moist column through 500mb leads to scattered snow showers ahead of the shortwave. Figure 3.1 depicts similiar cellular patterns between radars in the time-averaged  $Z_{eH}$  field. In contrast, the  $Z_{DR}$  comparison in Figure 3.2 shows that although the fields are similiar in their anisotropy, the spatial matching between the two is tenuous everywhere but in the heaviest showers. To investigate further, we examine a scatter-plot directly comparing matched values between radars. Artifacts are present in both moments in Figure 3.3, indicated by evenly spaced vertical lines; these indicate an anomaly originating from the axis of which they are normal to. For  $Z_{eH}$ , the artifacts are no longer present for values greater than 15 dBZ, which

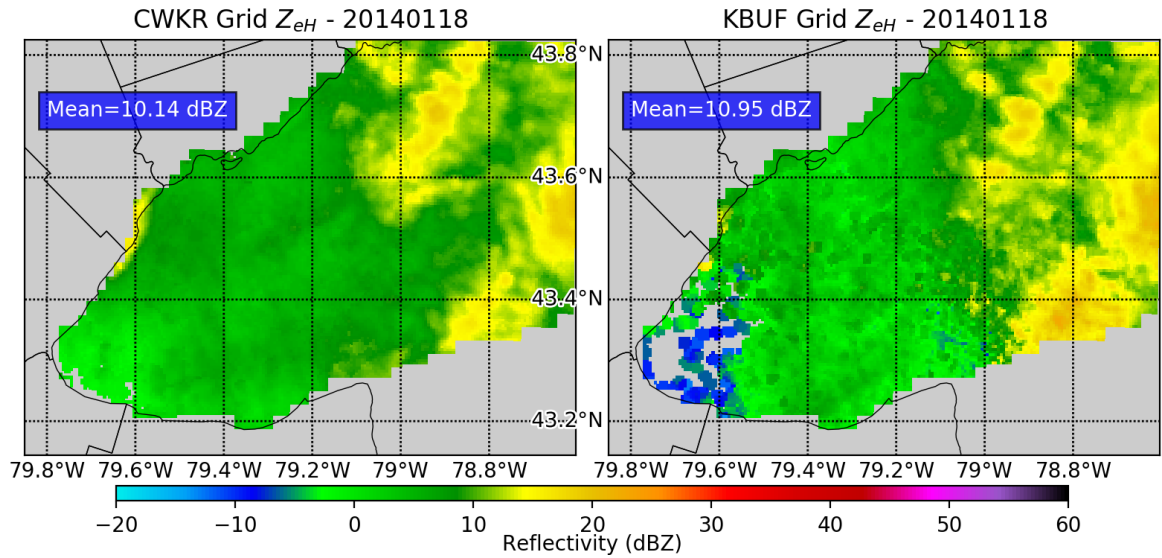


Figure 3.1: Gridded  $Z_{eH}$  comparison for 18 January 2014. Time-average of all admitted scans.

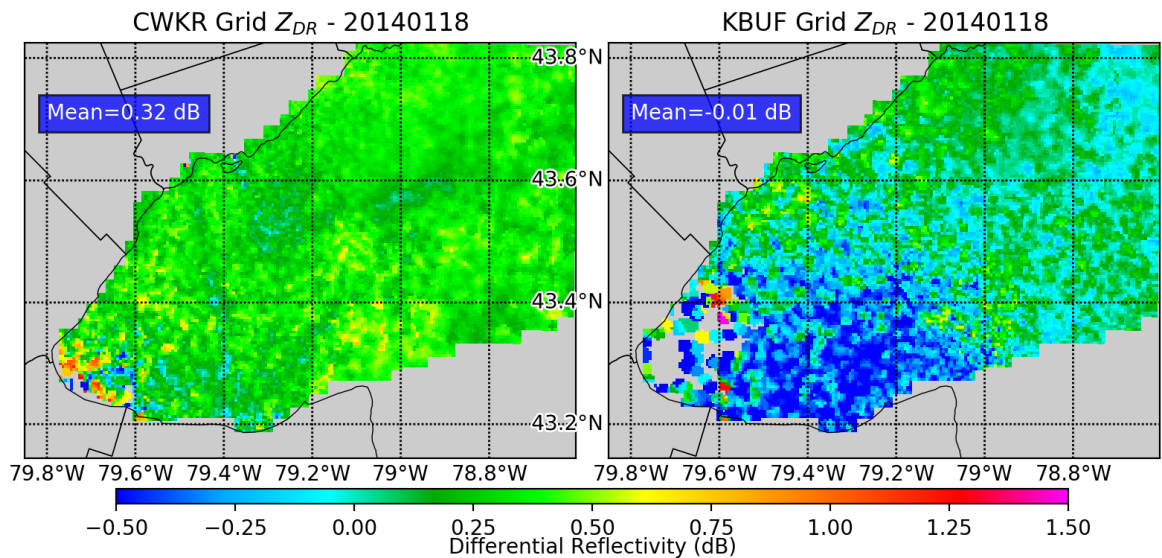


Figure 3.2: Gridded  $Z_{DR}$  comparison for 18 January 2014. Time-average of all admitted scans.

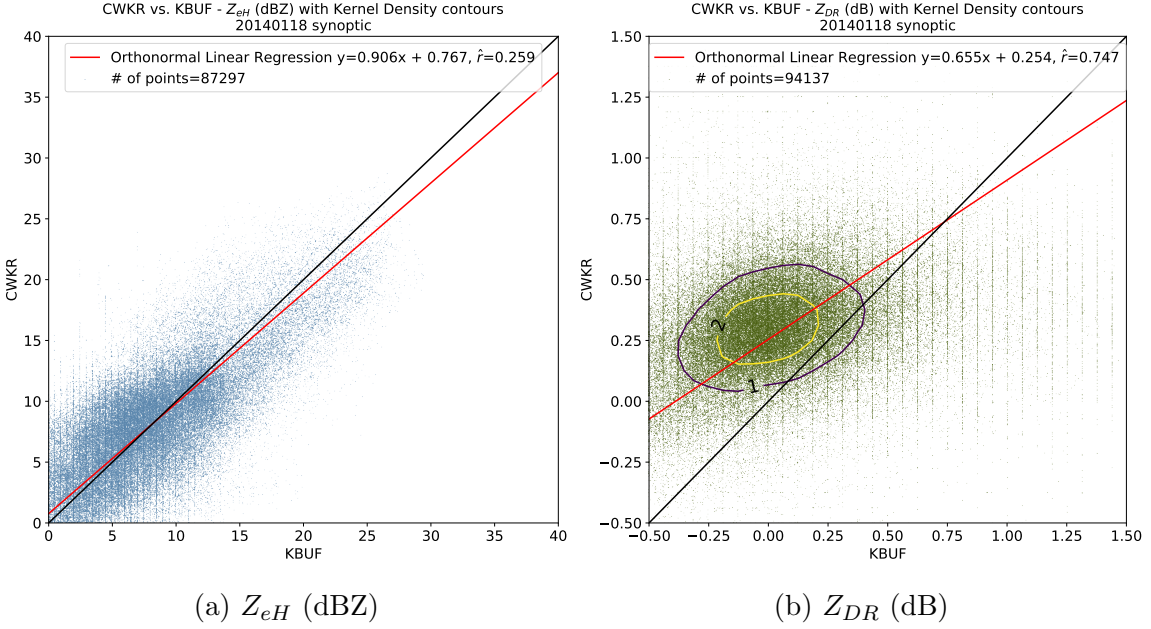


Figure 3.3: Direct comparisons for 18 January 2014. Dataset includes all admitted grid cells.

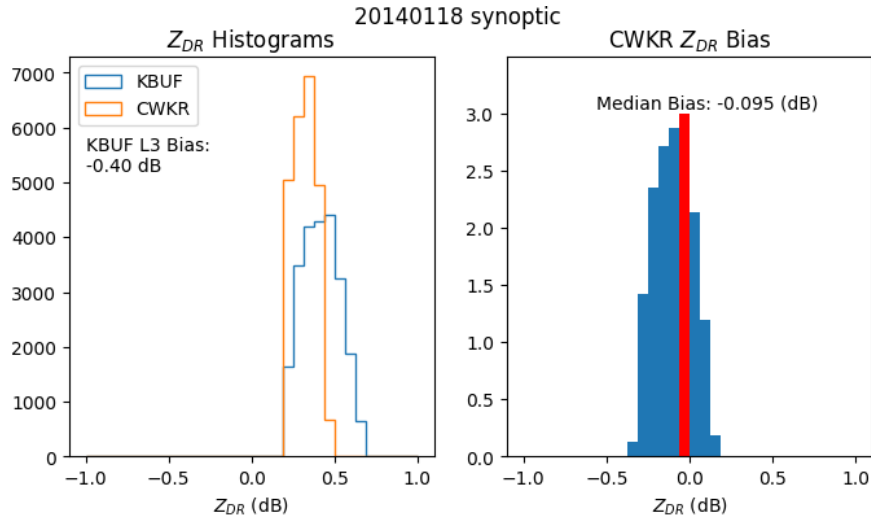


Figure 3.4: Histograms of  $Z_{DR}$  (left),  $Z_{DR}$  bias at CWKR, determined by subtracting the gridded, bias adjusted  $Z_{DR}$  at KBUF from the  $Z_{DR}$  at CWKR. Both datasets exclude matched points with  $KDE < 2$ .

indicates that a stronger weather signal leads to better matching. In  $Z_{DR}$  the artifacts are present throughout, but it is still possible to extract a signal from the noise. Data points with a normalized kernel density greater than two are selected for the determination of bias between radars. Figure 3.4 gives an estimate of the bias at CWKR, with a value of -0.095 dB. This indicates that no discernible bias exists within the error limit of  $\pm 0.1$  dB during this event.

### 3.1.2 23 January 2014 - Lake-Effect

A positively tilted longwave trough dominates the eastern third of Canada during this event, with NW winds at 850mb and SW winds at the surface. This light yet convergent flow yields the single, heavy band depicted in Figure 3.8, colloquially referred to as “tea-kettle” lake-effect snow. There is also a background stream of very light lake-effect snow impinging from Lake Erie. Spatial banding patterns of the lake-effect snow in the time-averaged  $Z_{eH}$  fields as compared between the radars are remarkably similar. In contrast, the  $Z_{DR}$  comparison indicates that although the fields are similar in their anisotropy, the spatial matching between the two is tenuous everywhere but in the heaviest showers. An anisotropic pattern is imparted on the  $Z_{DR}$  fields by the light snow from Lake Erie, evident in Figure 3.5. The scatter-plot in Figure ?? shows a good fit for  $Z_{eH}$  between radars, with the slope of the orthonormal  $a$  is still possible to extract a signal from the noise. Data points with a normalized kernel density greater than two are selected for the determination of bias between radars. Figure 3.7 gives an estimate of the bias at CWKR, with a value of -0.055 dB. Once again, no discernible bias exists within the error limit of  $\pm 0.1$  dB for this event.

### 3.1.3 1 February 2014 - Synoptic

This event is characterized by strong SW flow aloft, with above average moisture content. This leads to widespread stratiform snow, with an eventual transition to rain outside of the time interval selected.

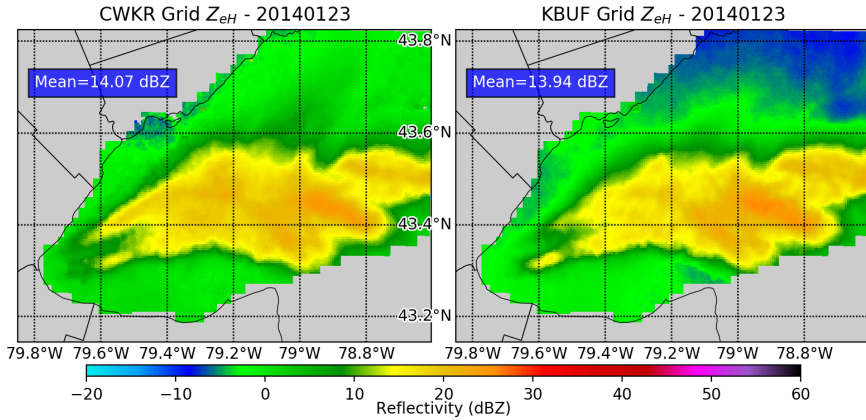


Figure 3.5: Gridded  $Z_{eH}$  comparison for 23 January 2014. Time-average of all admitted scans.

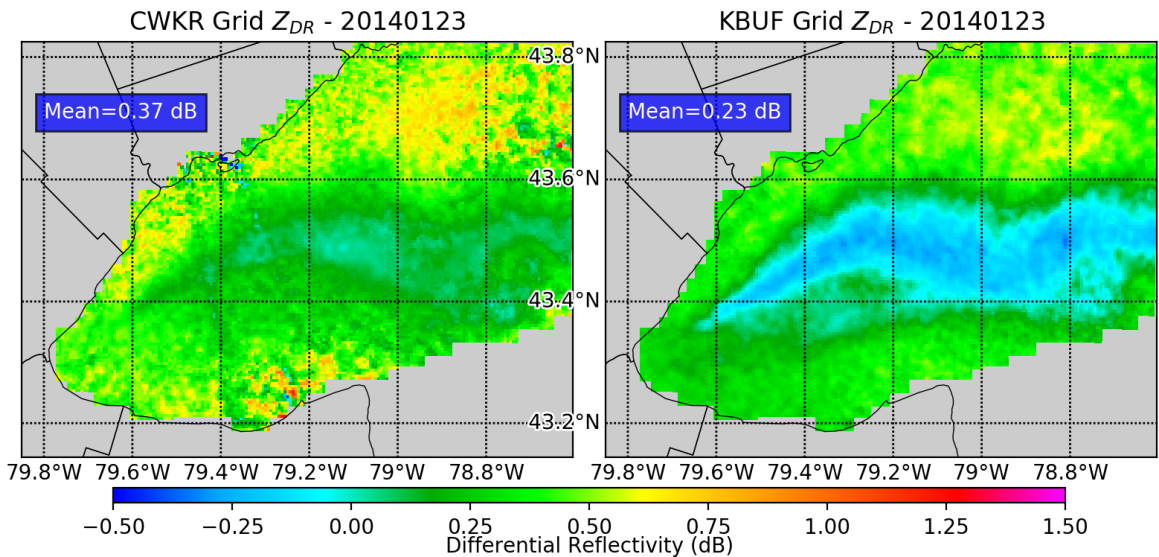


Figure 3.6: Gridded  $Z_{DR}$  comparison for 23 January 2014. Time-average of all admitted scans.

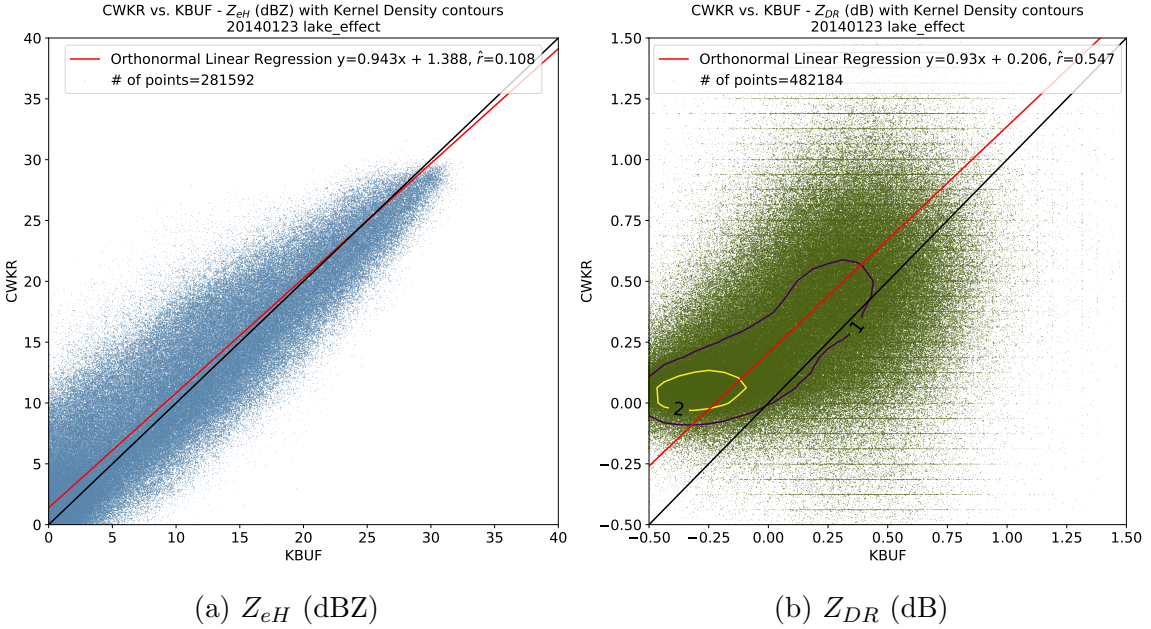


Figure 3.7: Direct comparisons for 23 January 2014. Dataset includes all admitted grid cells.

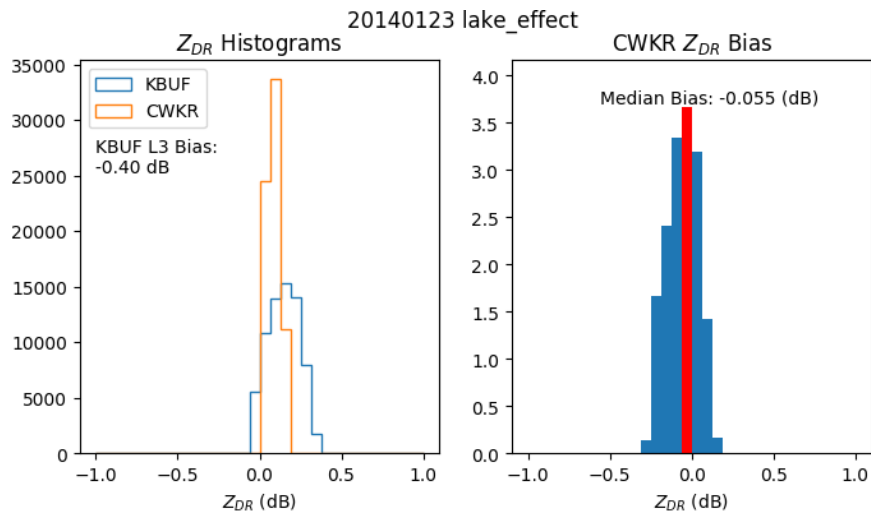


Figure 3.8: Histograms of  $Z_{DR}$  (left),  $Z_{DR}$  bias at CWKR, determined by subtracting the gridded, bias adjusted  $Z_{DR}$  at KBUF from the  $Z_{DR}$  at CWKR. Both datasets exclude matched points with KDE < 2.

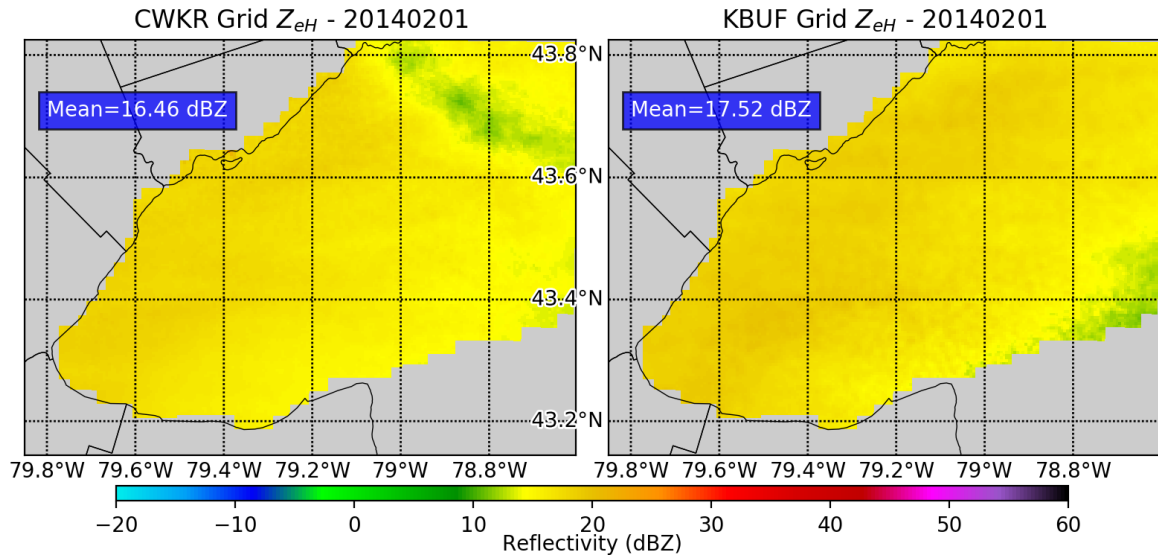


Figure 3.9: Gridded  $Z_{eH}$  comparison for 1 February 2014. Time-average of all admitted scans.

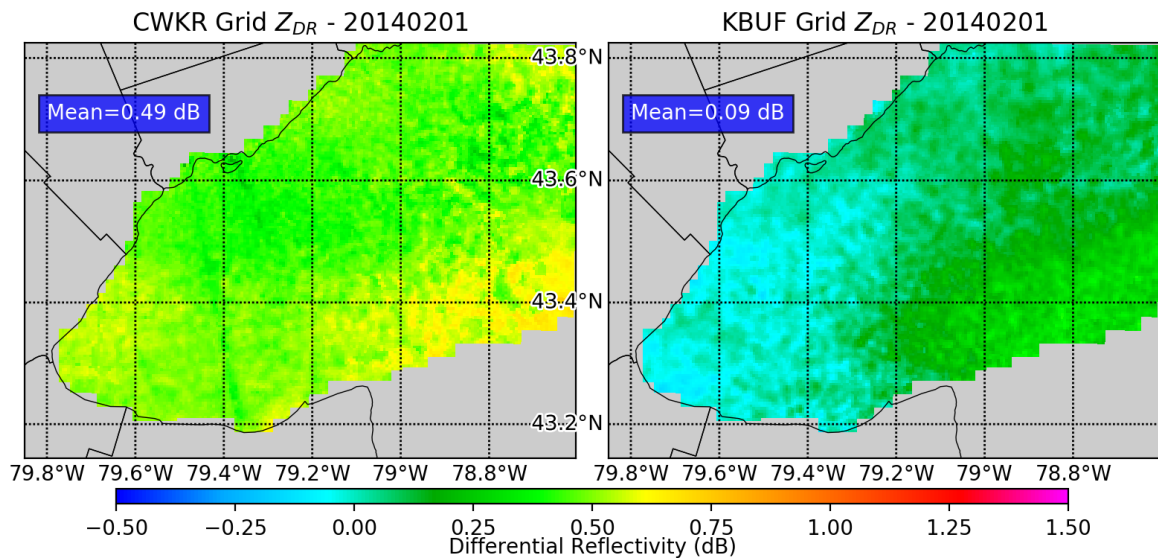


Figure 3.10: Gridded  $Z_{DR}$  comparison for 1 February 2014. Time-average of all admitted scans.

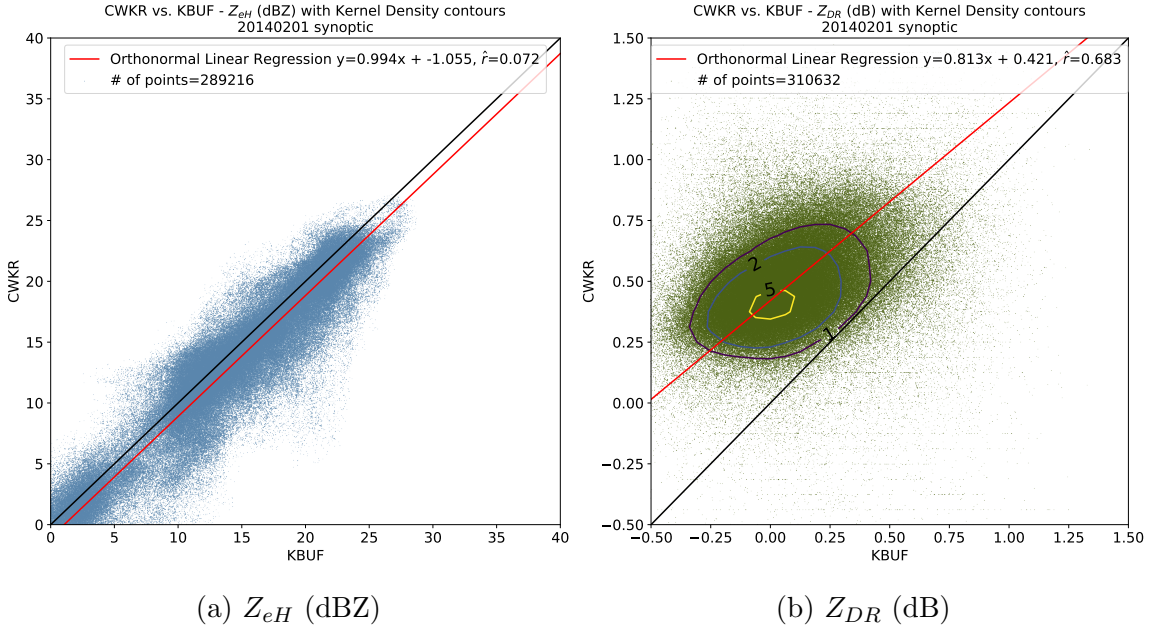


Figure 3.11: Direct comparisons for 1 February 2014. Dataset includes all admitted grid cells.

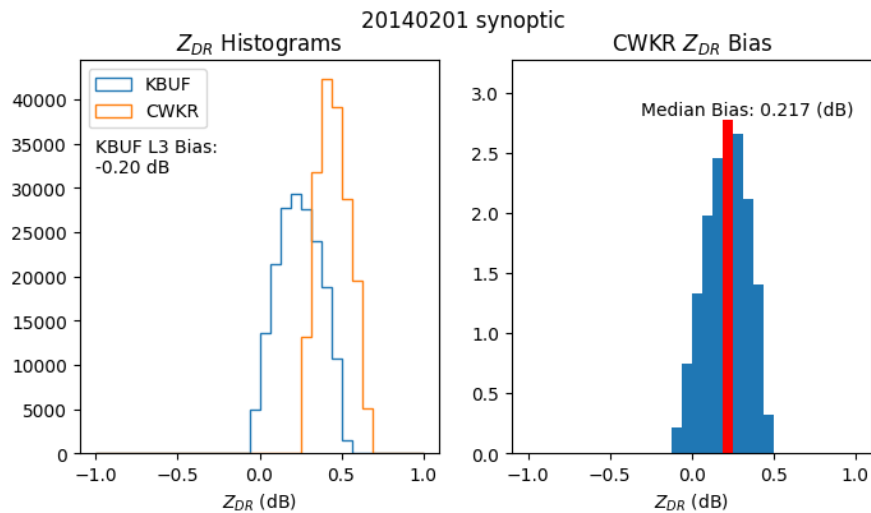


Figure 3.12: Histograms of  $Z_{DR}$  (left),  $Z_{DR}$  bias at CWKR, determined by subtracting the gridded, bias adjusted  $Z_{DR}$  at KBUF from the  $Z_{DR}$  at CWKR. Both datasets exclude matched points with KDE < 2.

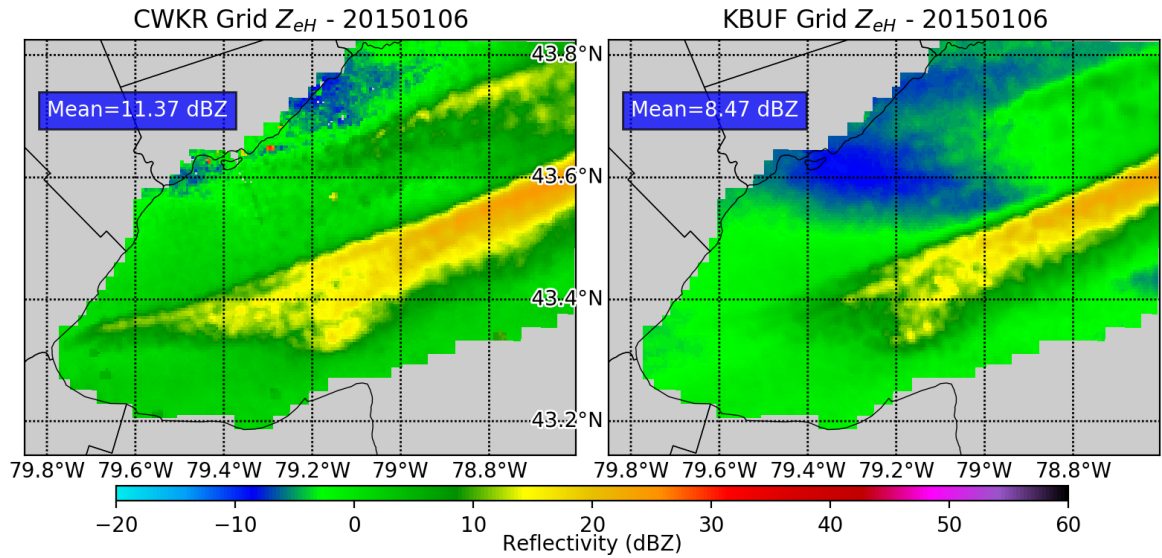


Figure 3.13: Gridded  $Z_{eH}$  comparison for 6 January 2015. Time-average of all admitted scans.

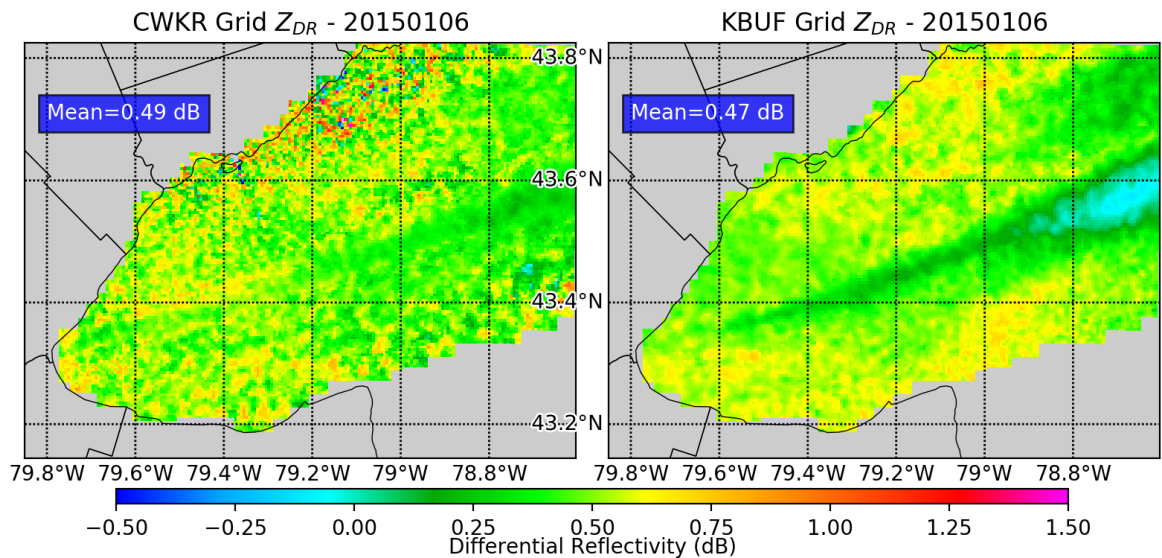


Figure 3.14: Gridded  $Z_{DR}$  comparison for 6 January 2015. Time-average of all admitted scans.

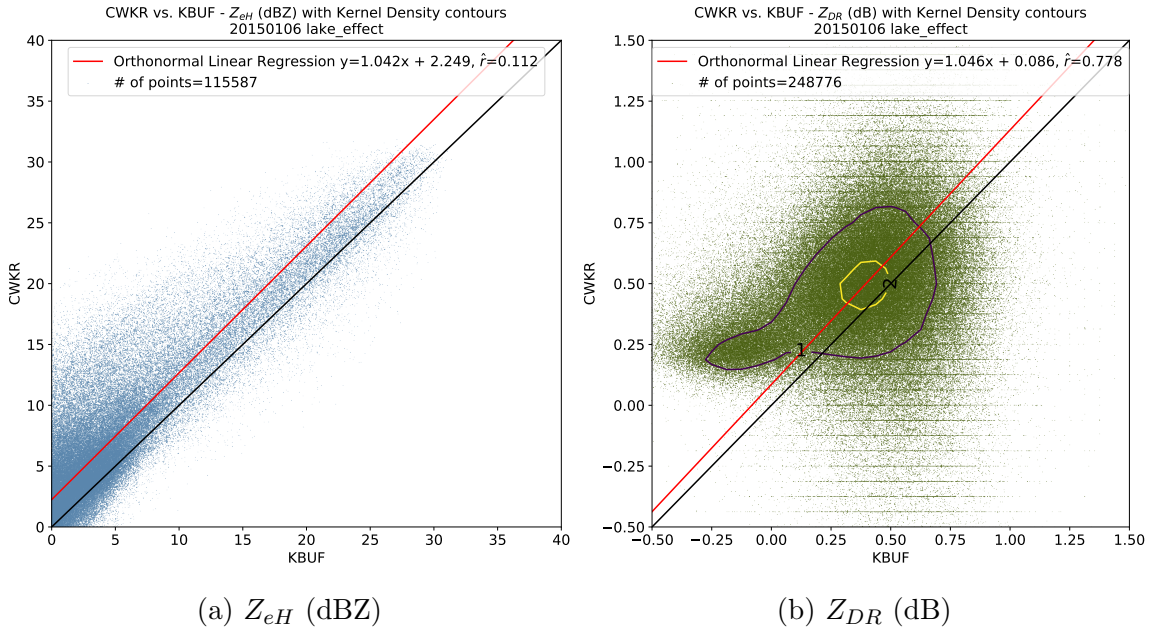


Figure 3.15: Direct comparisons for 6 January 2015. Dataset includes all admitted grid cells.

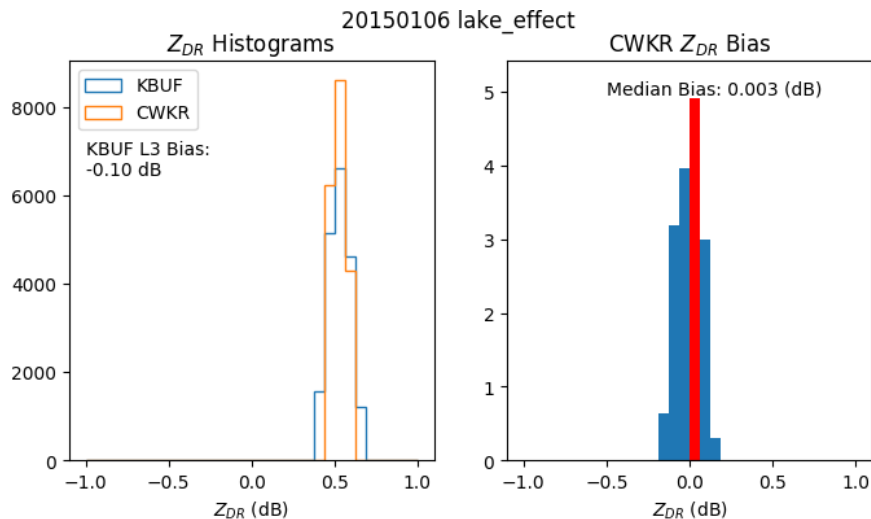


Figure 3.16: Histograms of  $Z_{DR}$  (left),  $Z_{DR}$  bias at CWKR, determined by subtracting the gridded, bias adjusted  $Z_{DR}$  at KBUF from the  $Z_{DR}$  at CWKR. Both datasets exclude matched points with KDE < 2.

### **3.1.4 6 January 2015 - Lake-Effect**

A highly zonal, NW flow aloft is present in this case, typical of lake-effect snow for the Great Lakes region. Anemic in radar appearance, a lake-effect band develops in the light winds near the surface; this case could be characterized as a weak “tea-kettle” event. Figure 3.13 depicts the time-averaged  $Z_{eH}$  during the event.

### **3.1.5 7 January 2015 - Synoptic**

Less than 24 hours after the previous event, the zonal flow has buckled and a strong shortwave is approaching Southern Ontario. Radar animations indicate a cold front passage over the lake occurs. Figure 3.17 shows a solid band of snow progressed from mid-lake southward.

### **3.1.6 6 February 2015 - Synoptic**

For this event, Southern Ontario is on the backside of shortwave, with a frontal passage occurring once again.

### **3.1.7 14 February 2015 - Lake-Effect**

While Southern Ontario is bracing for the impact of a bowling-ball like lobe of the polar vortex, strong W to SW flow from the surface to 850mb allows for a prolonged period of lake-effect snow over the lake.

### **3.1.8 18 February 2015 - Lake-Effect**

Four days later, The polar vortex has arrived in earnest for this event, with the 500 dm isoheight nearing as far south as Windsor, ON. The cold airmass allows for the development of an intense lake-effect snow band, the strongest of all the lake-effect cases as indicated by the  $Z_{eH}$  means in Figure 3.29.

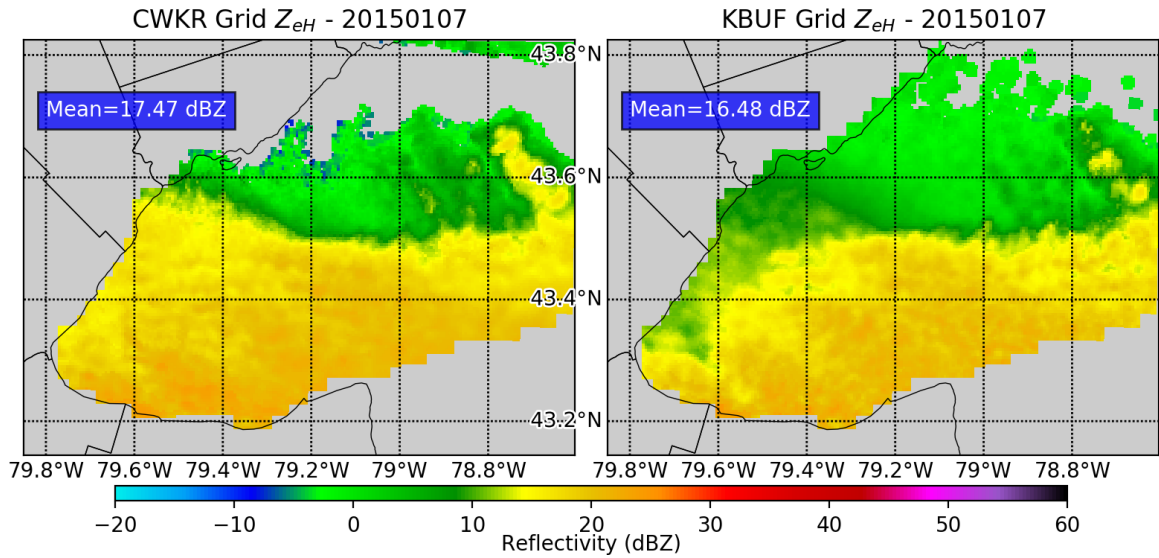


Figure 3.17: Gridded  $Z_{eH}$  comparison for 7 January 2015. Time-average of all admitted scans.

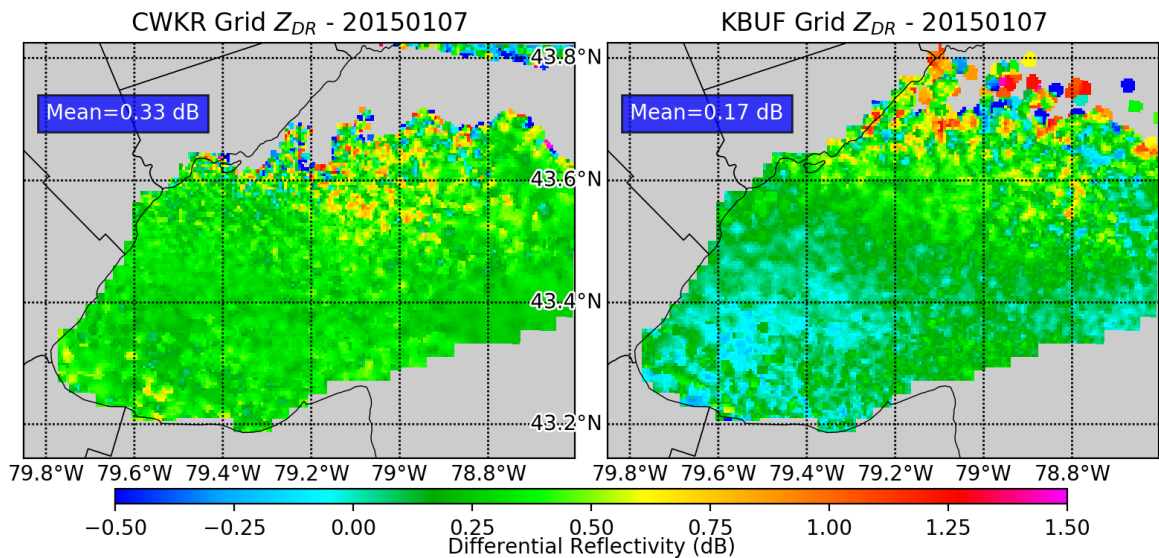


Figure 3.18: Gridded  $Z_{DR}$  comparison for 7 January 2015. Time-average of all admitted scans.

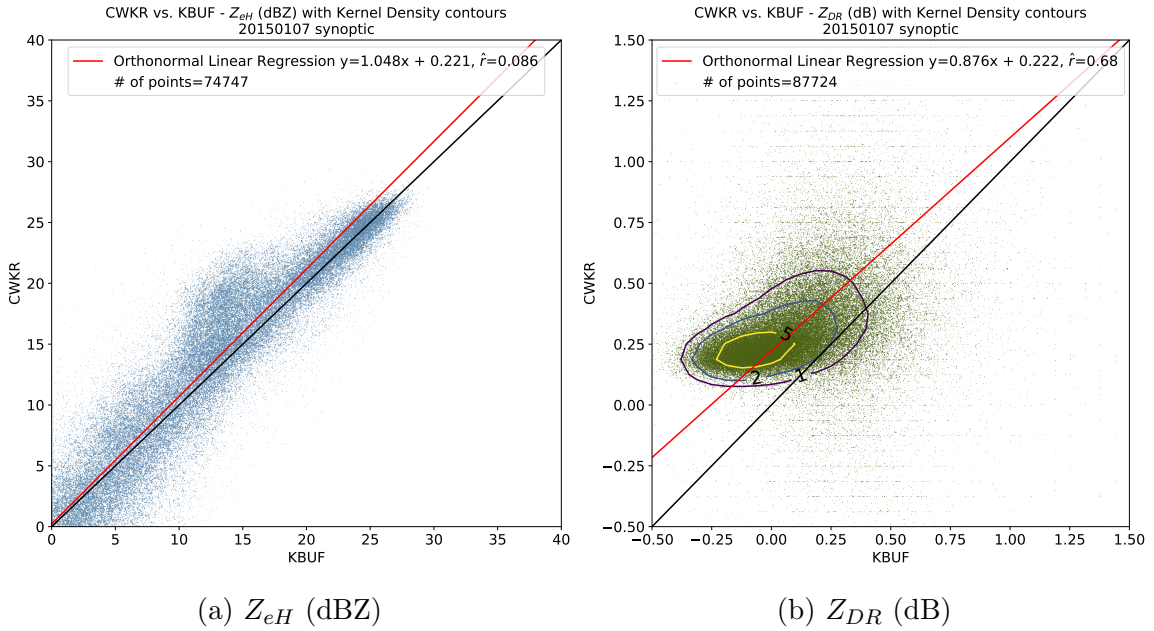


Figure 3.19: Direct comparisons for 7 January 2015. Dataset includes all admitted grid cells.

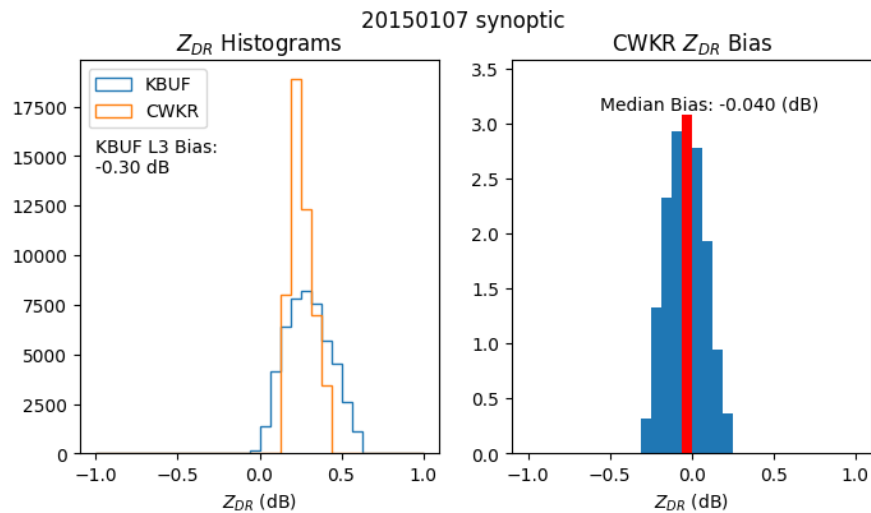


Figure 3.20: Histograms of  $Z_{DR}$  (left),  $Z_{DR}$  bias at CWKR, determined by subtracting the gridded, bias adjusted  $Z_{DR}$  at KBUF from the  $Z_{DR}$  at CWKR. Both datasets exclude matched points with KDE < 2.

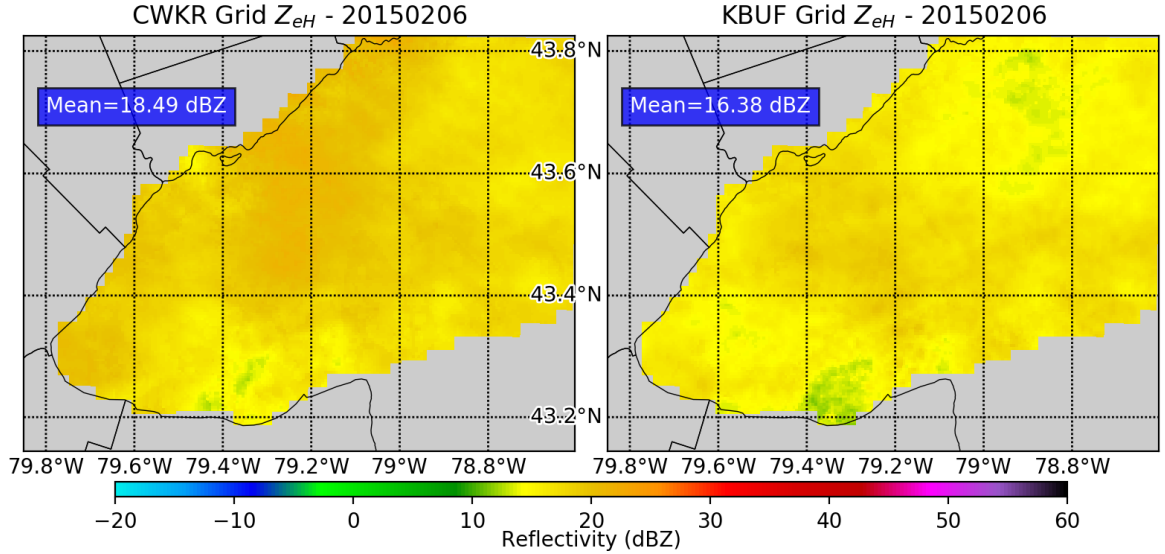


Figure 3.21: Gridded  $Z_{eH}$  comparison for 6 February 2015. Time-average of all admitted scans.

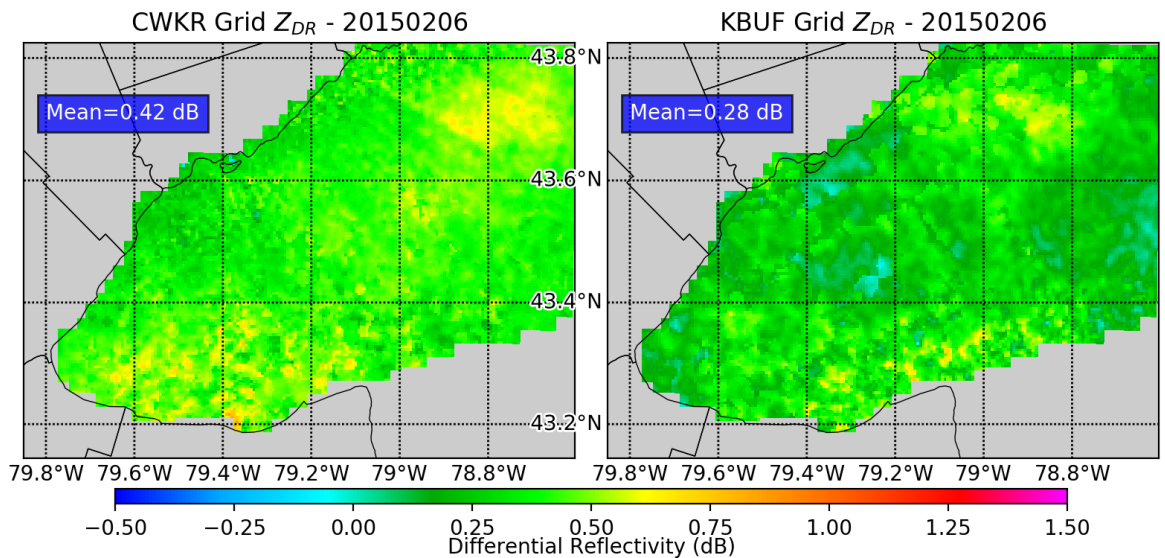


Figure 3.22: Gridded  $Z_{DR}$  comparison for 6 February 2015. Time-average of all admitted scans.

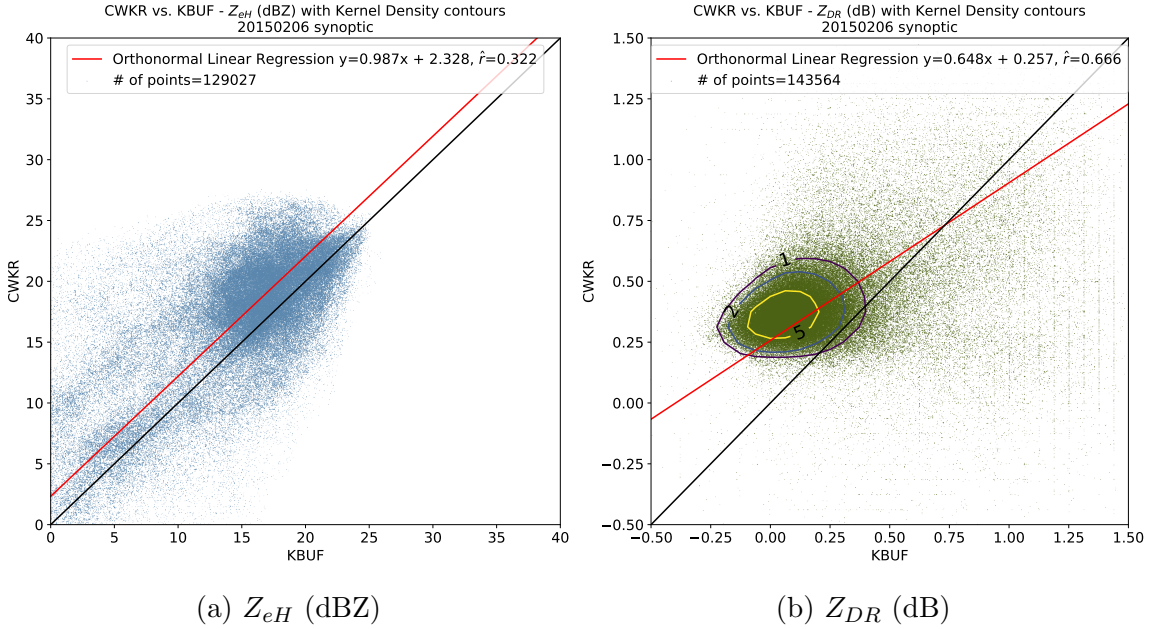


Figure 3.23: Direct comparisons for 6 February 2015. Dataset includes all admitted grid cells.

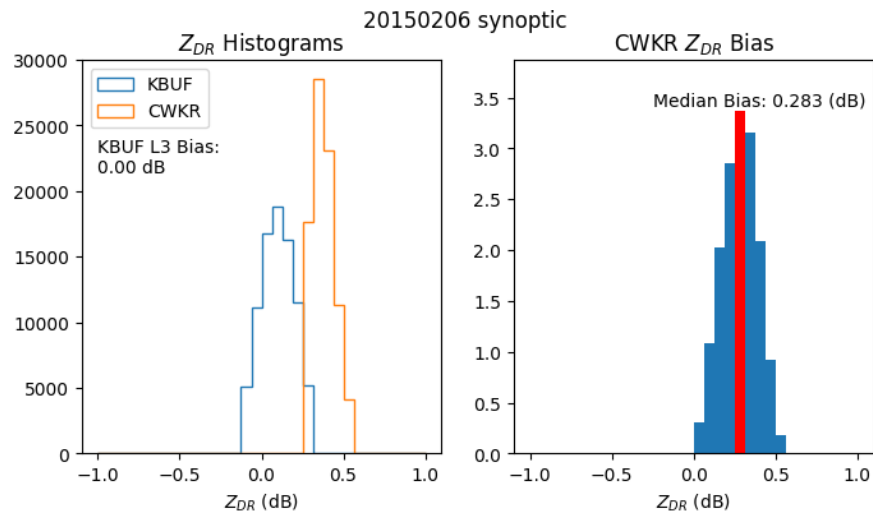


Figure 3.24: Histograms of  $Z_{DR}$  (left),  $Z_{DR}$  bias at CWKR, determined by subtracting the gridded, bias adjusted  $Z_{DR}$  at KBUF from the  $Z_{DR}$  at CWKR. Both datasets exclude matched points with KDE < 2.

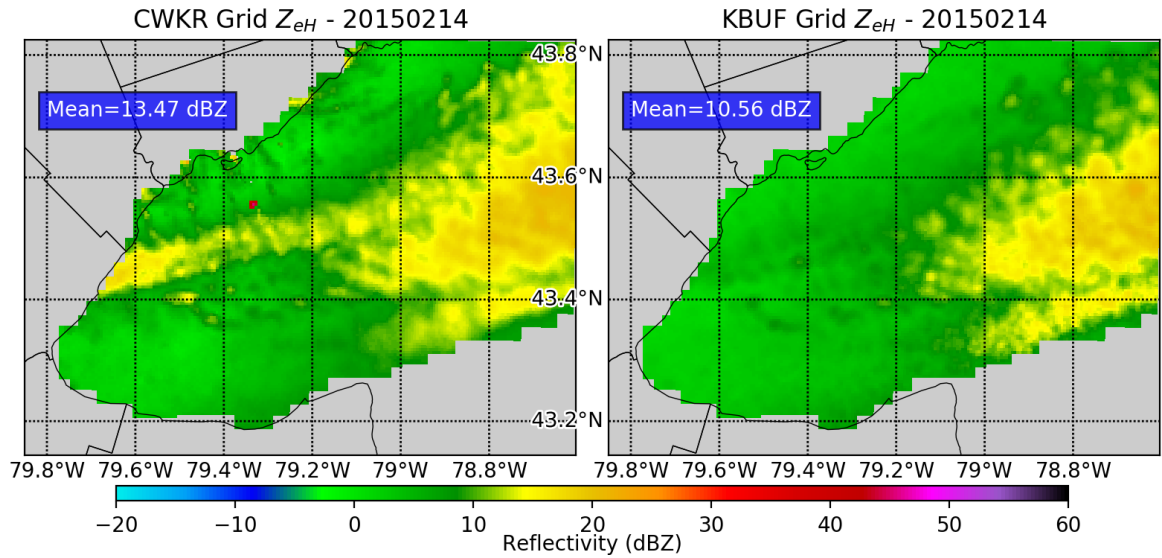


Figure 3.25: Gridded  $Z_{eH}$  comparison for 14 February 2015. Time-average of all admitted scans.

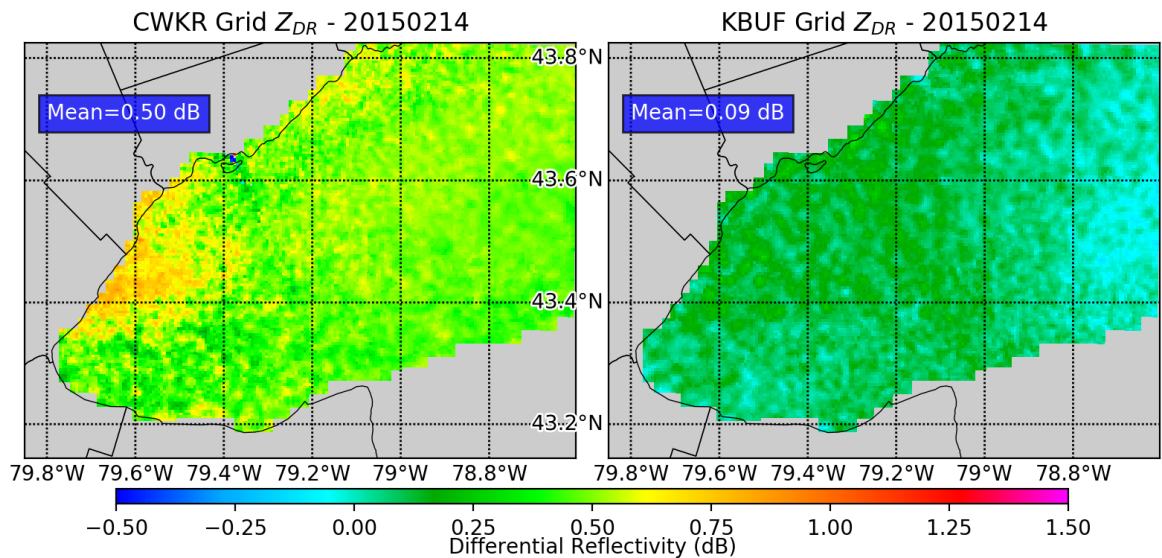


Figure 3.26: Gridded  $Z_{DR}$  comparison for 14 February 2015. Time-average of all admitted scans.

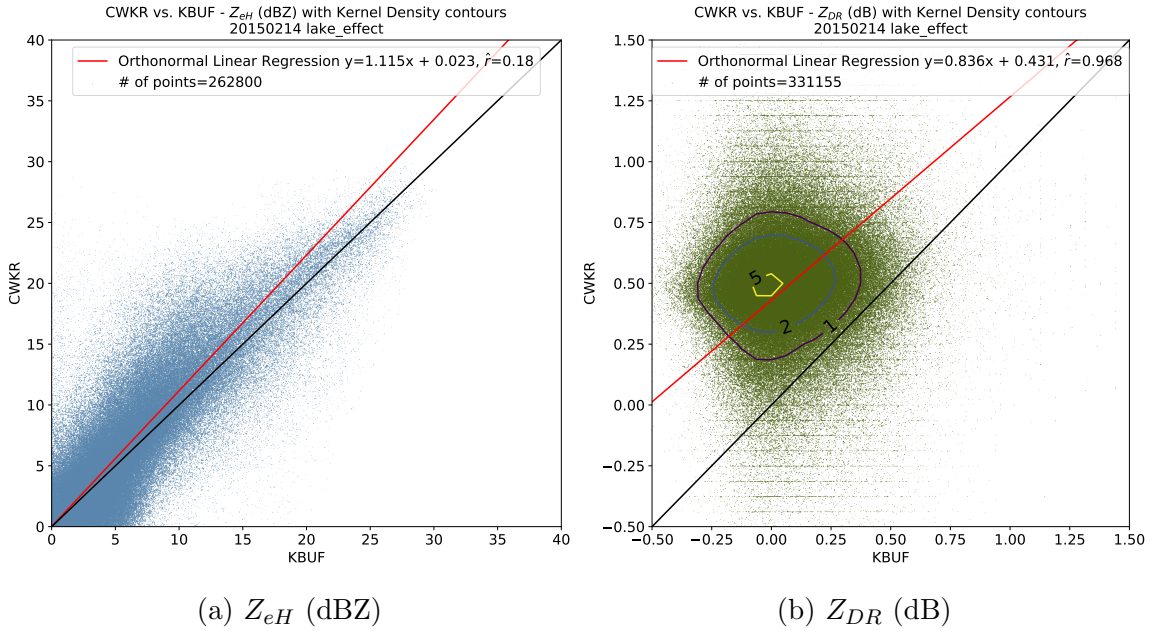


Figure 3.27: Direct comparisons for 14 February 2015. Dataset includes all admitted grid cells.

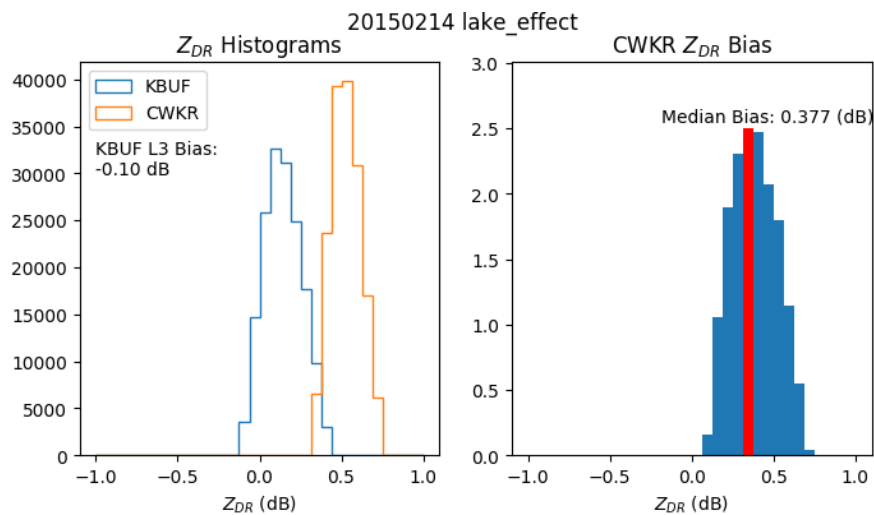


Figure 3.28: Histograms of  $Z_{DR}$  (left),  $Z_{DR}$  bias at CWKR, determined by subtracting the gridded, bias adjusted  $Z_{DR}$  at KBUF from the  $Z_{DR}$  at CWKR. Both datasets exclude matched points with KDE < 2.

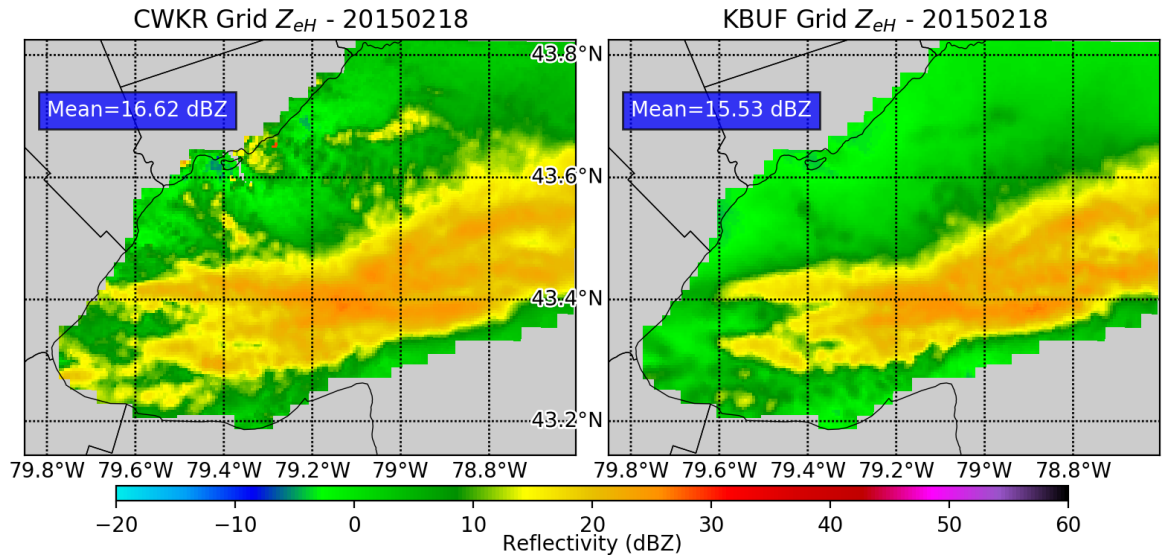


Figure 3.29: Gridded  $Z_{eH}$  comparison for 18 February 2015. Time-average of all admitted scans.

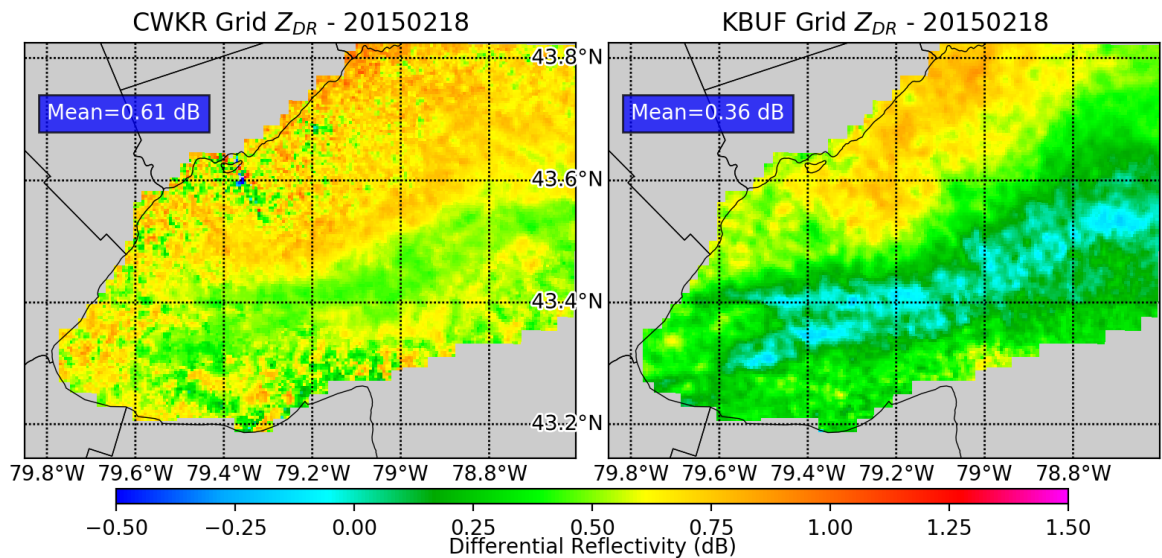


Figure 3.30: Gridded  $Z_{DR}$  comparison for 18 February 2015. Time-average of all admitted scans.

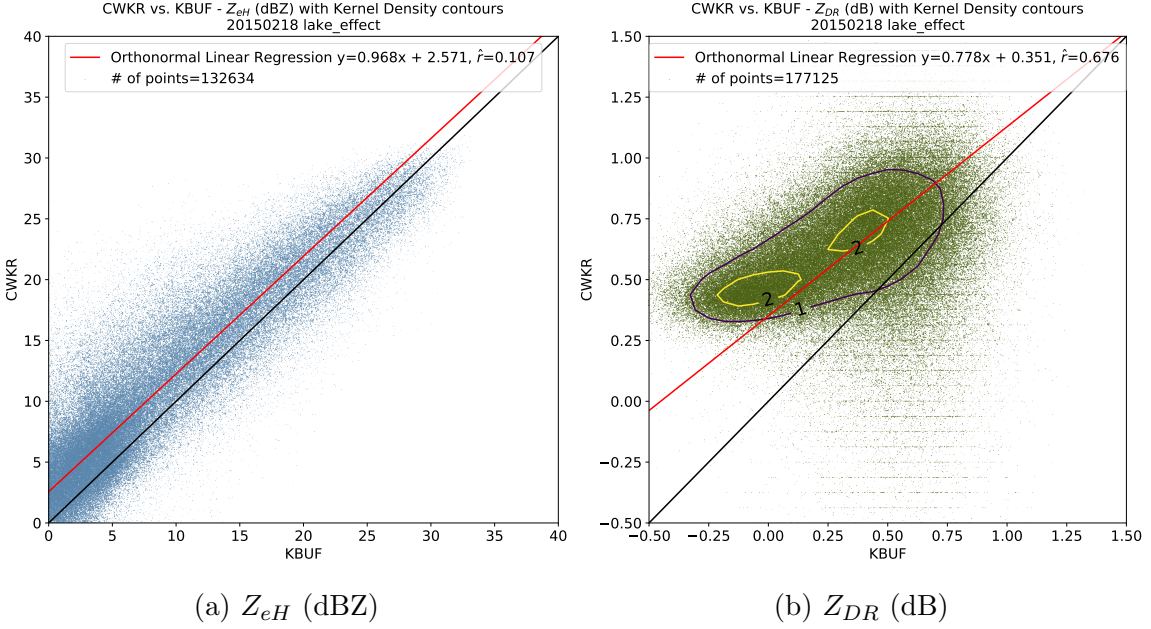


Figure 3.31: Direct comparisons for 18 February 2015. Dataset includes all admitted grid cells.

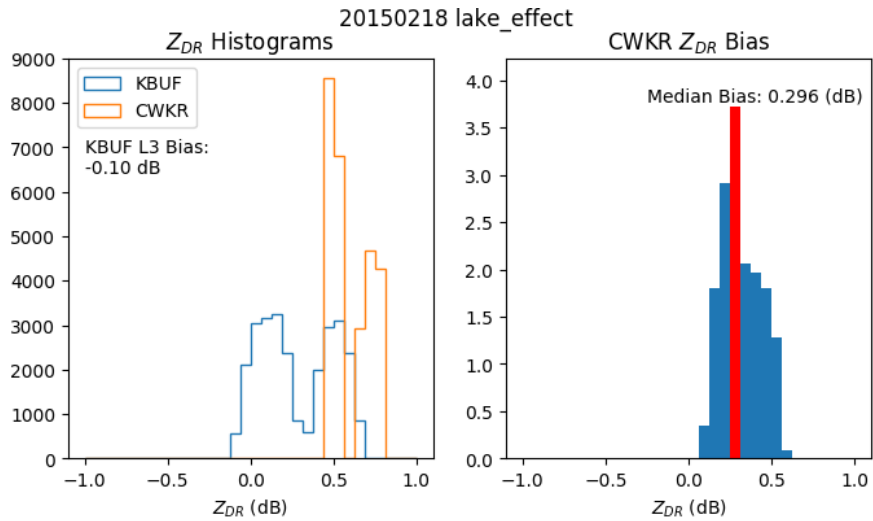


Figure 3.32: Histograms of  $Z_{DR}$  (left),  $Z_{DR}$  bias at CWKR, determined by subtracting the gridded, bias adjusted  $Z_{DR}$  at KBUF from the  $Z_{DR}$  at CWKR. Both datasets exclude matched points with KDE < 2.

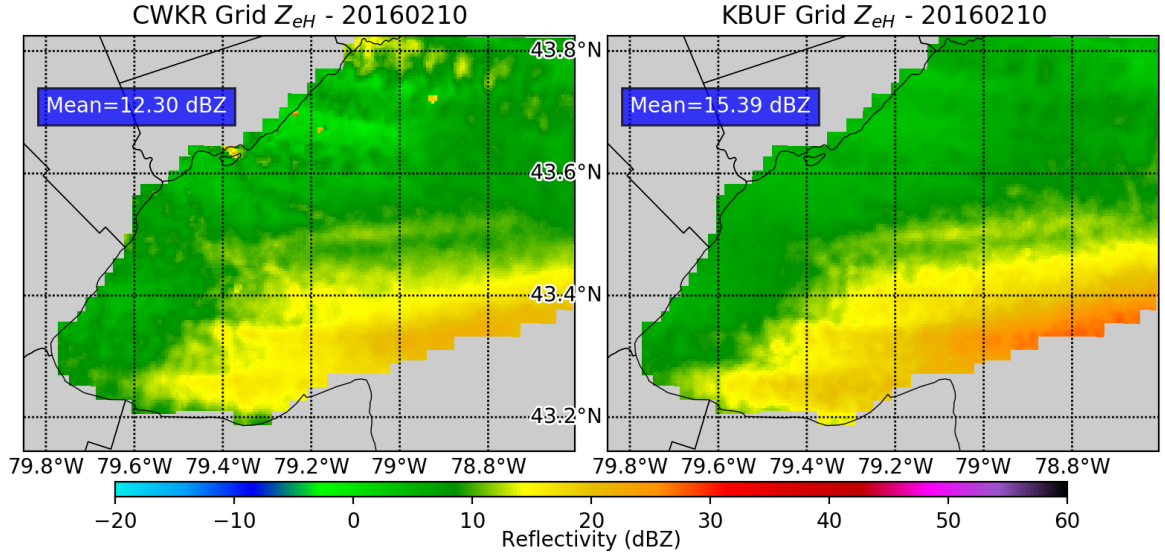


Figure 3.33: Gridded  $Z_{eH}$  comparison for 10 February 2016. Time-average of all admitted scans.

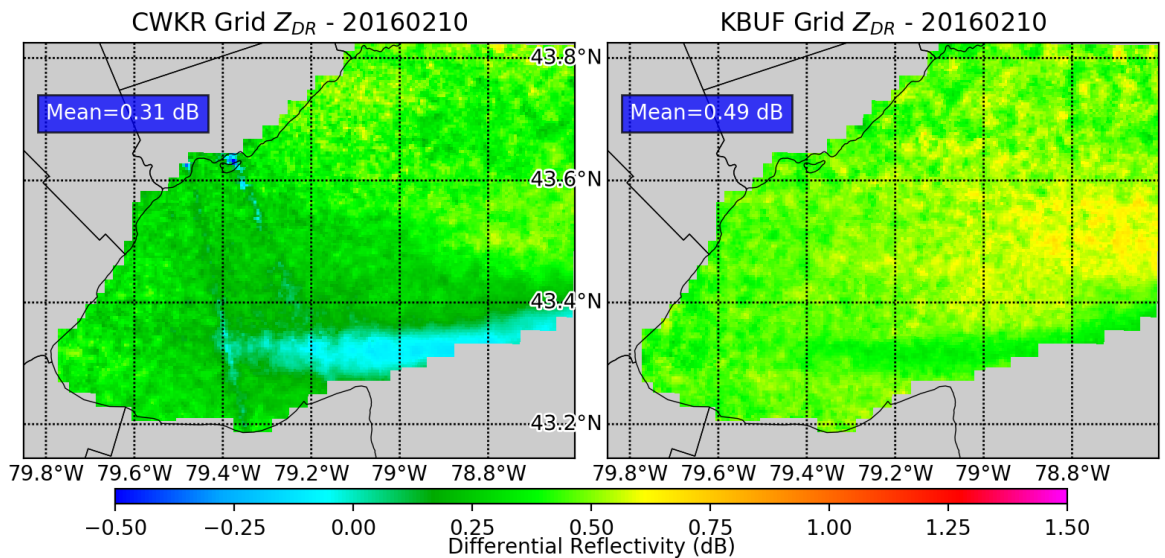


Figure 3.34: Gridded  $Z_{DR}$  comparison for 10 February 2016. Time-average of all admitted scans.

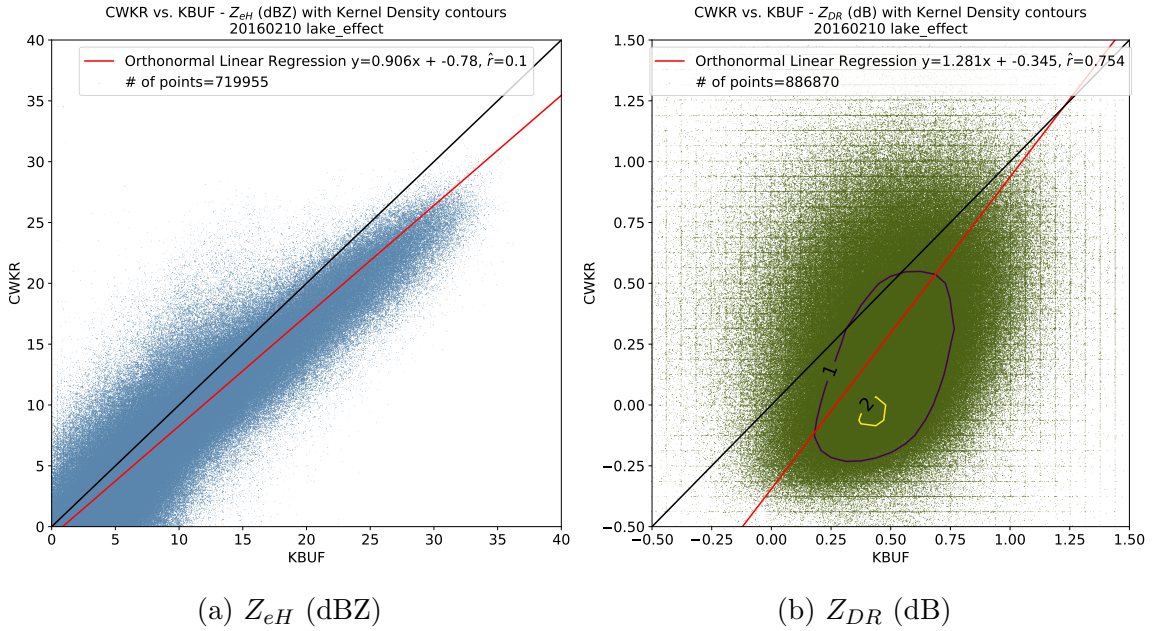


Figure 3.35: Direct comparisons for 10 February 2016. Dataset includes all admitted grid cells.

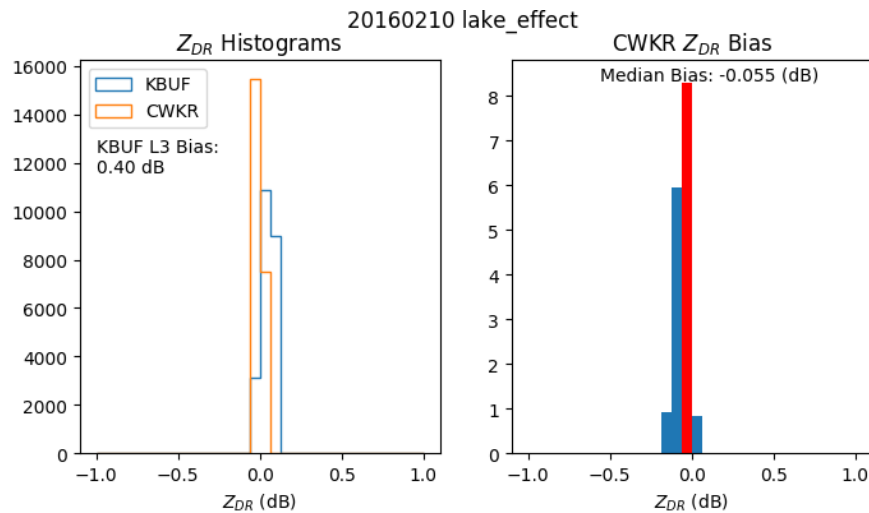


Figure 3.36: Histograms of  $Z_{DR}$  (left),  $Z_{DR}$  bias at CWKR, determined by subtracting the gridded, bias adjusted  $Z_{DR}$  at KBUF from the  $Z_{DR}$  at CWKR. Both datasets exclude matched points with KDE < 2.

### **3.1.9 10 February 2016 - Lake-Effect**

The 500mb ridge axis is centered to the south of Southern Ontario in the Appalachians, with WNW flow aloft during this event. With a slight amount of pre-existing instability augmenting the lake induced instabilities, a healthy band of convection forms on the southern end of the lake. non-existent directional shear from the surface to 850mb

### **3.1.10 15 December 2016 - Synoptic**

A deep longwave trough is centered over Southern Ontario, within an Arctic airmass in place over the Great Lakes region. With meager moisture in place, a post-frontal trough manages to squeeze out some passing snow-showers, indicated in Figure 3.37.

### **3.1.11 $Z_{eH}$ Subset Direct Comparisons**

The first direct comparisons are shown in Figure 3.41, with a scatter-plot of KBUF  $Z_{eH}$  data versus CWKR on the common grid. Figure 3.41a is the subset of synoptic events while Figure 3.41b is the subset of lake-effect events. These results show that lake-effect snow events achieve a better match between the radars than synoptic events; there is a sample size caveat due to synoptic subset only containing about a third of the matched points than those in the synoptic subset. Another result shown in Figure 3.41 is that CWKR is slightly under-reporting reflectivity in the 15-25 dBZ range for lake-effect events, while it over-reports for synoptic events. In order to examine this further, we turn to Figure 3.42, revealing heavier banding closer to KBUF (south of 43.4° N and east of 79° W) in lake-effect events. Due to the bands location farther away from CWKR, its beam is most likely overshooting this shallow lake effect band. This is confirmed by the pattern in the reflectivity differences, which reveals a stronger range dependency in lake-effect events than synoptic. Another notable feature in Figure 3.42 is the resolution of finer scale features by CWKR is superior, especially for the lake-effect banding patterns around mid-lake. This is likely a function of its narrower physical beamwidth.

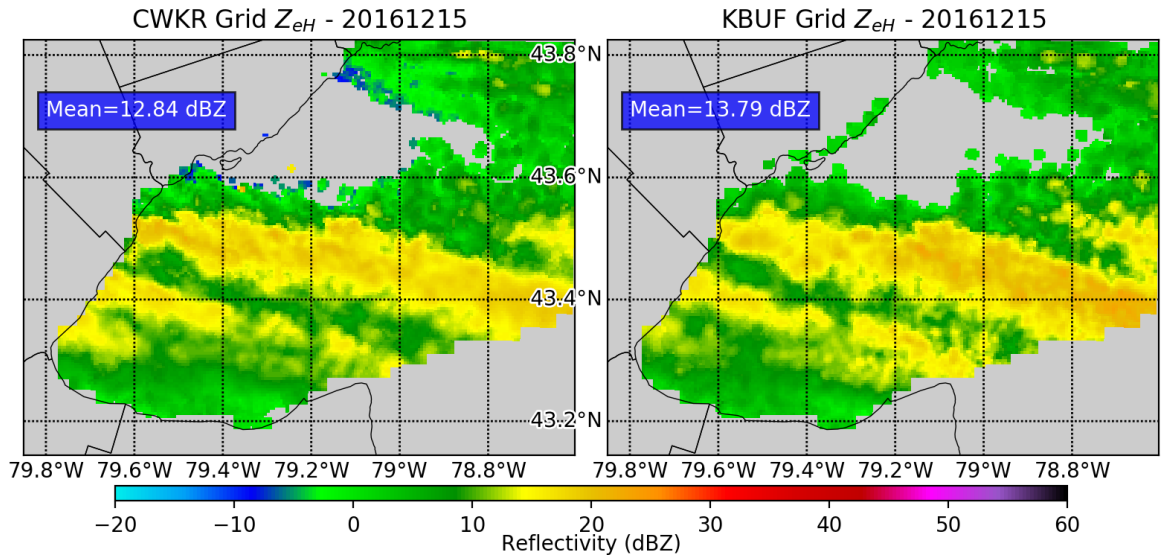


Figure 3.37: Gridded  $Z_{eH}$  comparison for 15 December 2016. Time-average of all admitted scans.

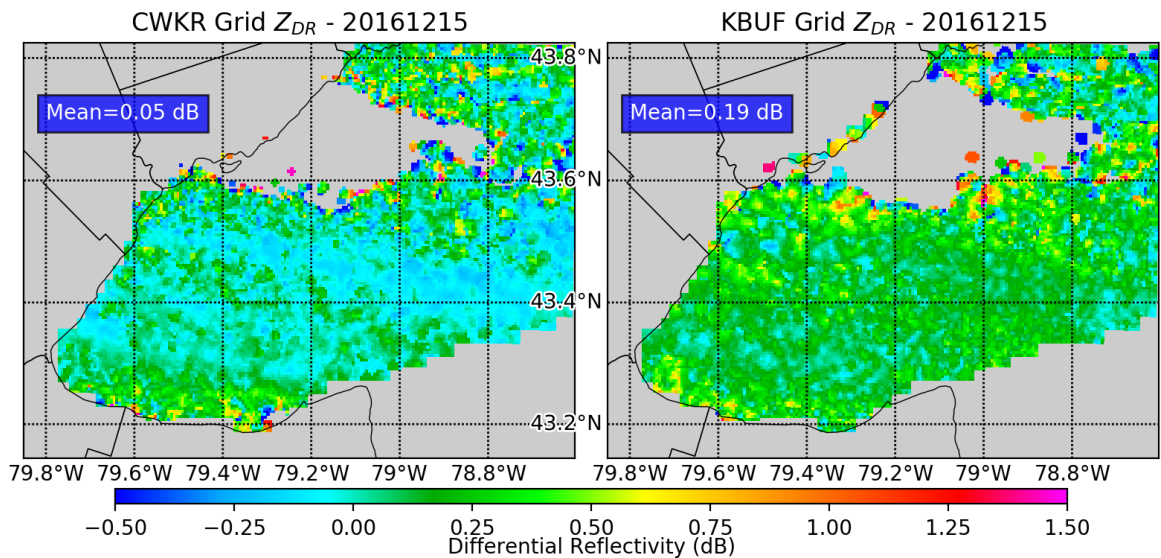


Figure 3.38: Gridded  $Z_{DR}$  comparison for 15 December 2016. Time-average of all admitted scans.

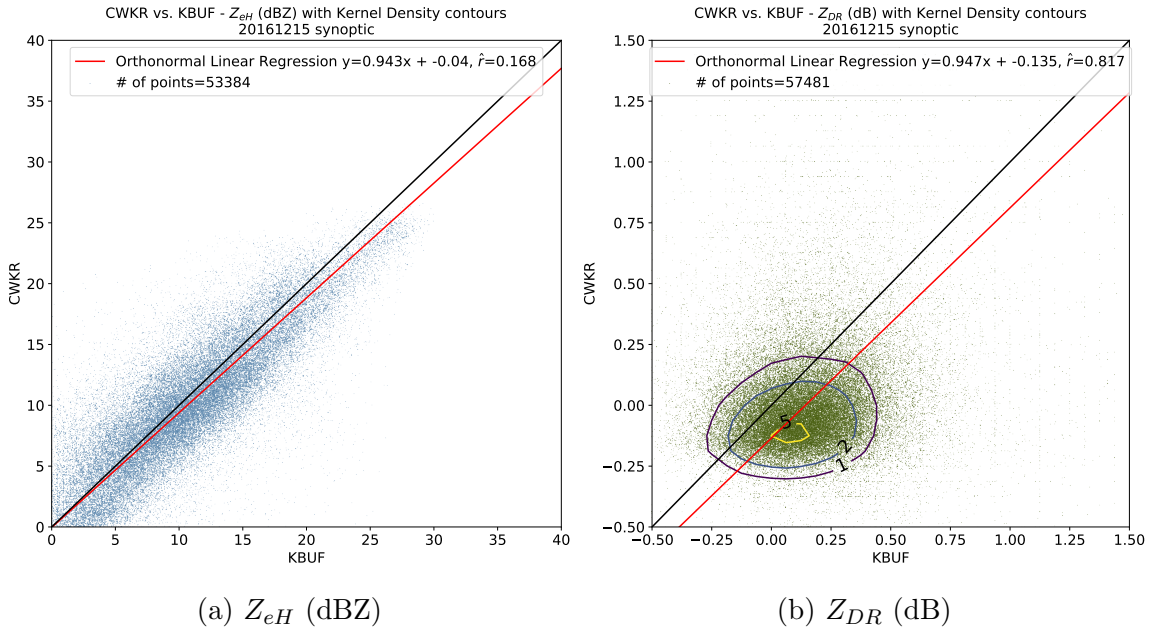


Figure 3.39: Direct comparisons for 15 December 2016. Dataset includes all admitted grid cells.

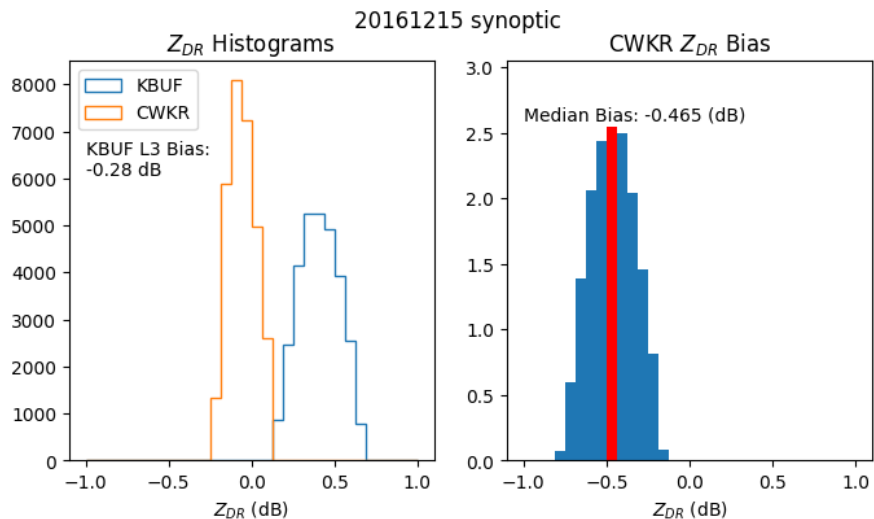


Figure 3.40: Histograms of  $Z_{DR}$  (left),  $Z_{DR}$  bias at CWKR, determined by subtracting the gridded, bias adjusted  $Z_{DR}$  at KBUF from the  $Z_{DR}$  at CWKR. Both datasets exclude matched points with KDE < 2.

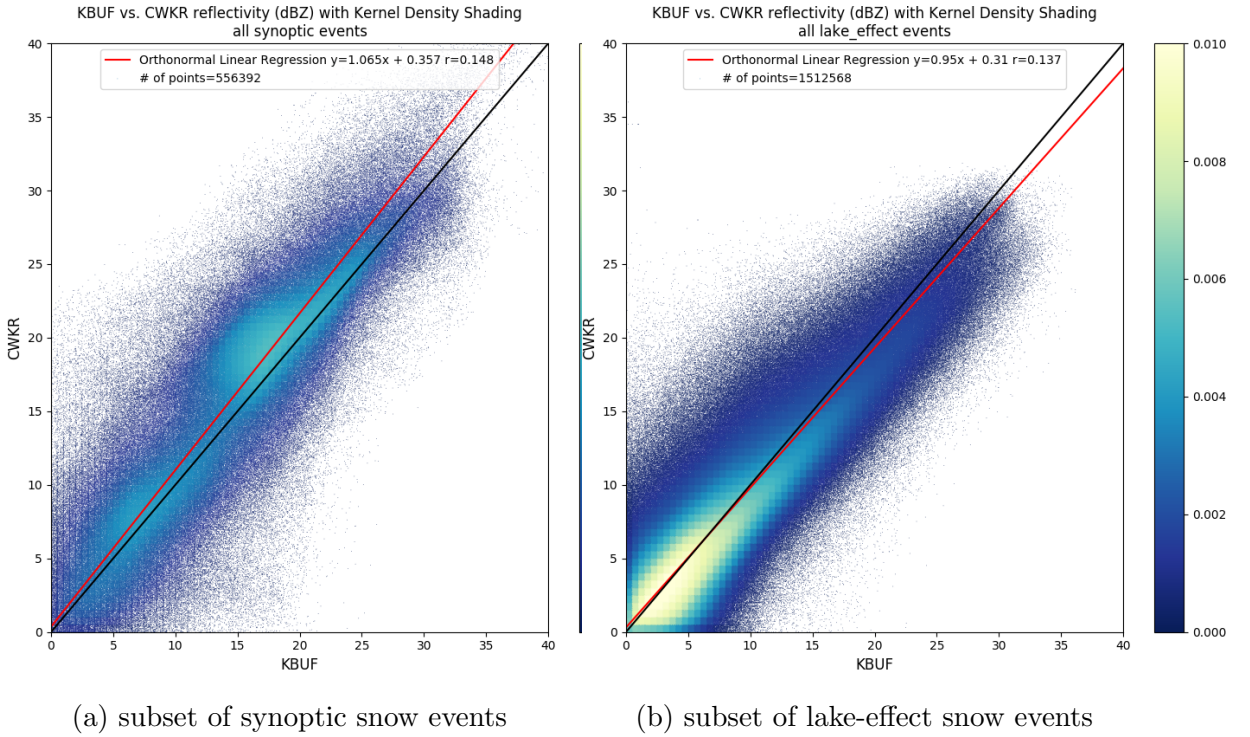


Figure 3.41: Scatter-plots of CWKR versus KBUF grid analyzed reflectivity, with Kernel Density Estimation shading. The red line is an Orthonormal Linear Regression, with a black identity line.

To investigate this further, we turn to a NEXRAD Level III algorithm which estimates  $Z_{DR}$  biases using external targets, as discussed by Cunningham et al. (2013). For the first lake-effect snow event on 23 January 2014, the  $Z_{DR}$  bias estimate at KBUF from the rain and snow methods shown in Figure 3.44 is approximately -0.4 dB, as given by the seven-day running median. This compares well with the bias estimate made by comparing KBUF with CWKR with all hydrometeor classes admitted, shown in Figure ???. When only dry snow bins are admitted though, the bias becomes masked, with Figure ?? showing a bias of nearly 0 dB. Figure ?? gives an example of a period when the radar is fixed and comes back into calibration. In contrast, during a synoptic snowfall event on 9 February 2014, Figure reffig:20140209hist shows that the dry snow filtering technique yields the best estimate of bias.

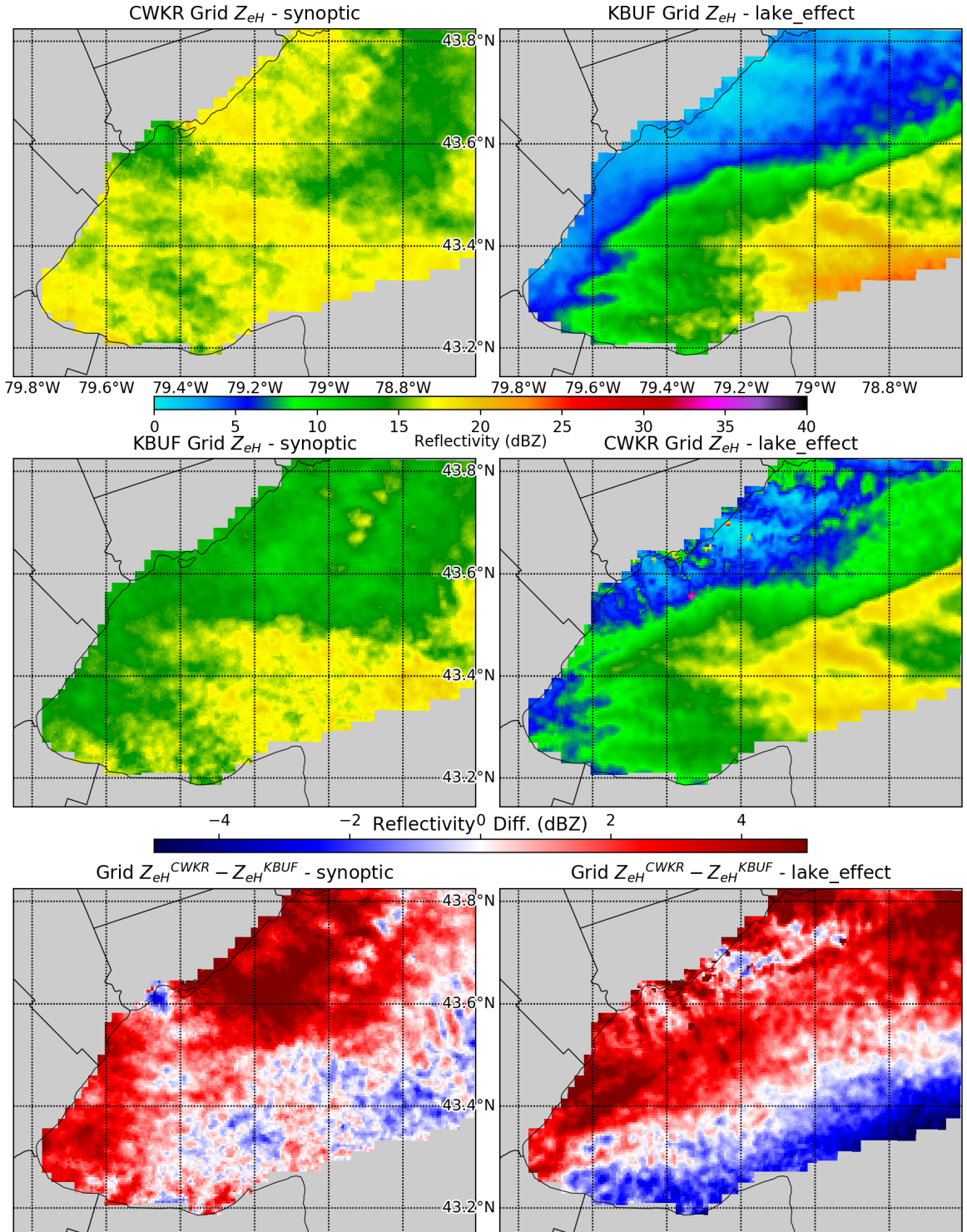


Figure 3.42: Time averaged subsets of grid  $Z_{eH}$  for KBUF and CWKR, with differences between the radars for each subset shown in the bottom panel.

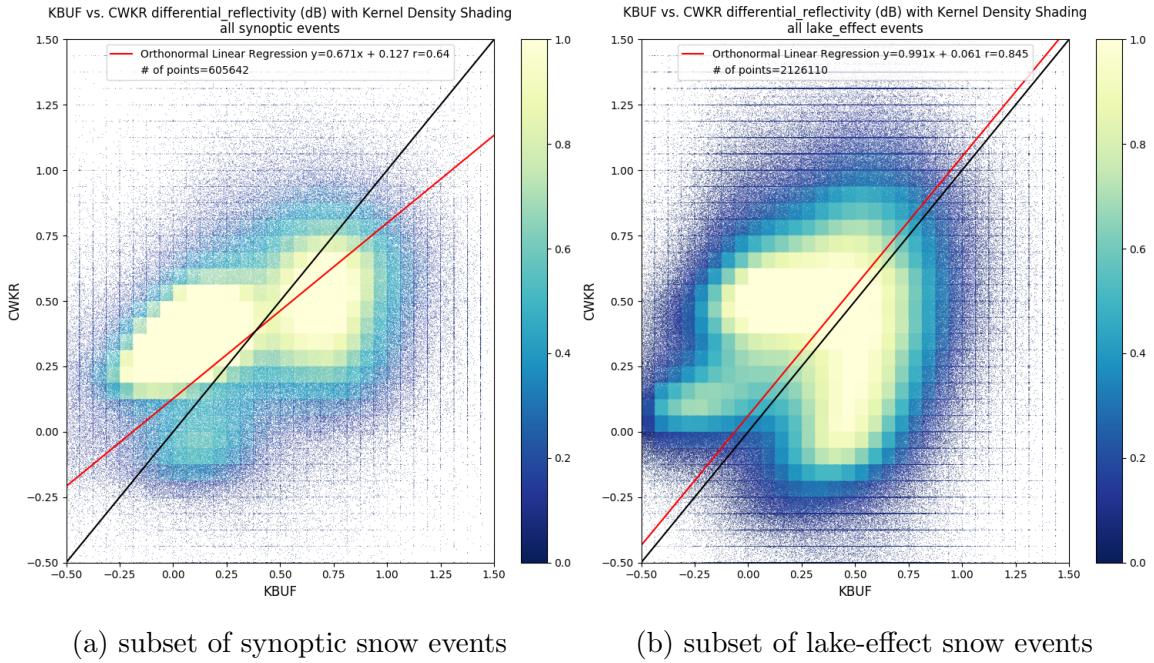


Figure 3.43: Scatter-plots of CWKR versus KBUF grid analyzed differential reflectivity, with Kernel Density Estimation shading. The red line is an Orthonormal Linear Regression, with a black identity line.

### 3.1.12 $Z_{DR}$ Subset Direct Comparison

When comparing  $Z_{DR}$  in the same manner as  $Z_{eH}$ , no clear pattern emerges. The analyzed values are highly uncorrelated, as shown in Figure 3.43. Unlike reflectivity, differential reflectivity is a relative quantity, and is much more sensitive to biases. Therefore, each case will be considered individually to estimate an event bias, if any. The externally estimated  $Z_{DR}$  bias from KBUF is subtracted out to give the bias at CWKR.

## 3.2 Initial Results

The main advantage of the common grid is that it allows for direct one-to-one comparison between the two radars. By directly interrogating the base moments, the veracity of the analysis technique is ensured, and any artifacts are identifiable. This will also help characterize differences between lake-effect and synoptic snow events,



KBUF\_bias\_2014\_jan-march.png

Figure 3.44: Graphs of KBUF January-March 2014  $Z_{DR}$  bias estimates from NEXRAD rain (top panel) and snow (bottom panel) methods. Shading is a seven-day running median and points are daily median values. Tolerance levels are shaded light blue from  $\pm 0.2$  dB. It is shown here that KBUF is outside of calibration tolerances. Data collected from archived NEXRAD Level III data.

in terms of objective analyzability and performance of the radar systems in resolving snowfall at meso- $\beta$  length scales versus synoptic length scales. As these are direct comparisons of radar data, hereafter the terms under(over)-reporting will be used to describe an estimate one radar makes in comparison with the other.

# **A Appendix A**

## **A.1 Upper-Air Charts**

Images provided by the NOAA/ESRL Physical Science Division, Boulder, Colorado.

Original data can be found at <http://www.esrl.noaa.gov/psd/>.

## **A.2 Skew-T Charts**

Raw sounding data provided by the Department of Atmospheric Science at the University of Wyoming. Original data can be found at <http://weather.uwyo.edu/upperair/sounding.html>.

## **A.3 Sounding Climatology**

Images provided by the National Weather Service Storm Prediction Center in Norman, Oklahoma. Original data can be found at <http://www.spc.noaa.gov/exper/soundingclimo/>.

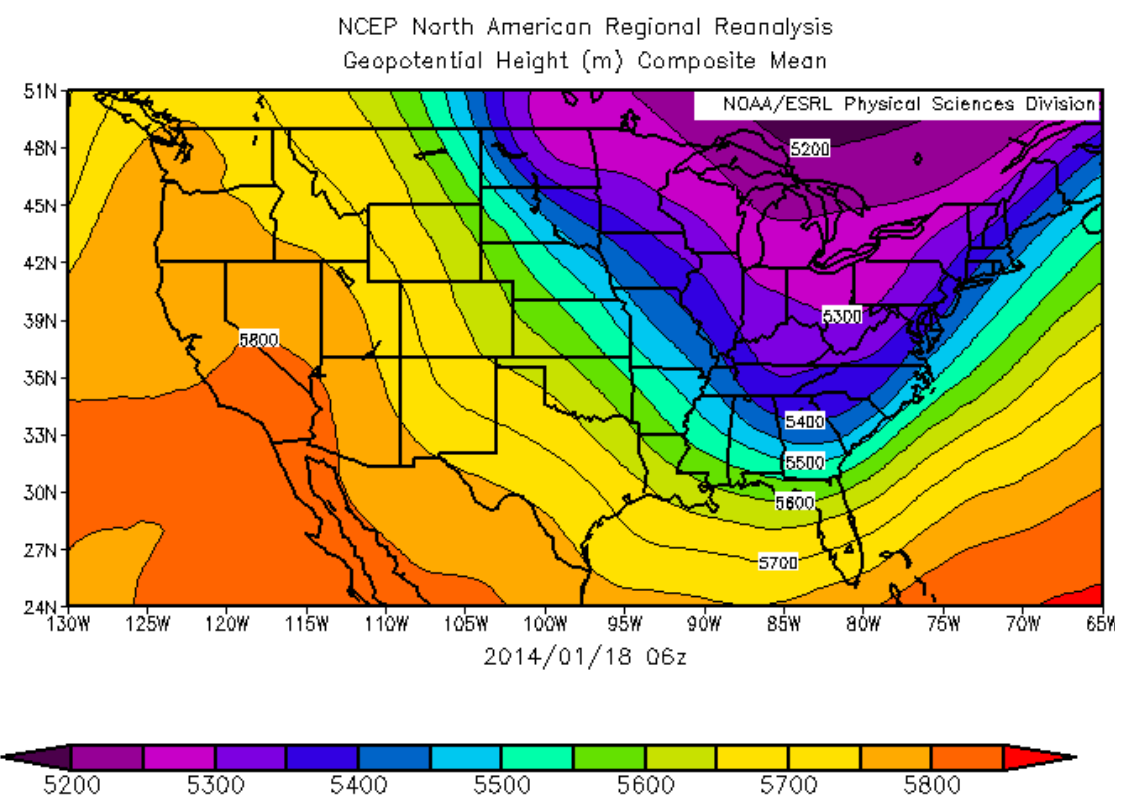


Figure A.1: 500mb Geopotential Height at 06Z 18 January 2014.

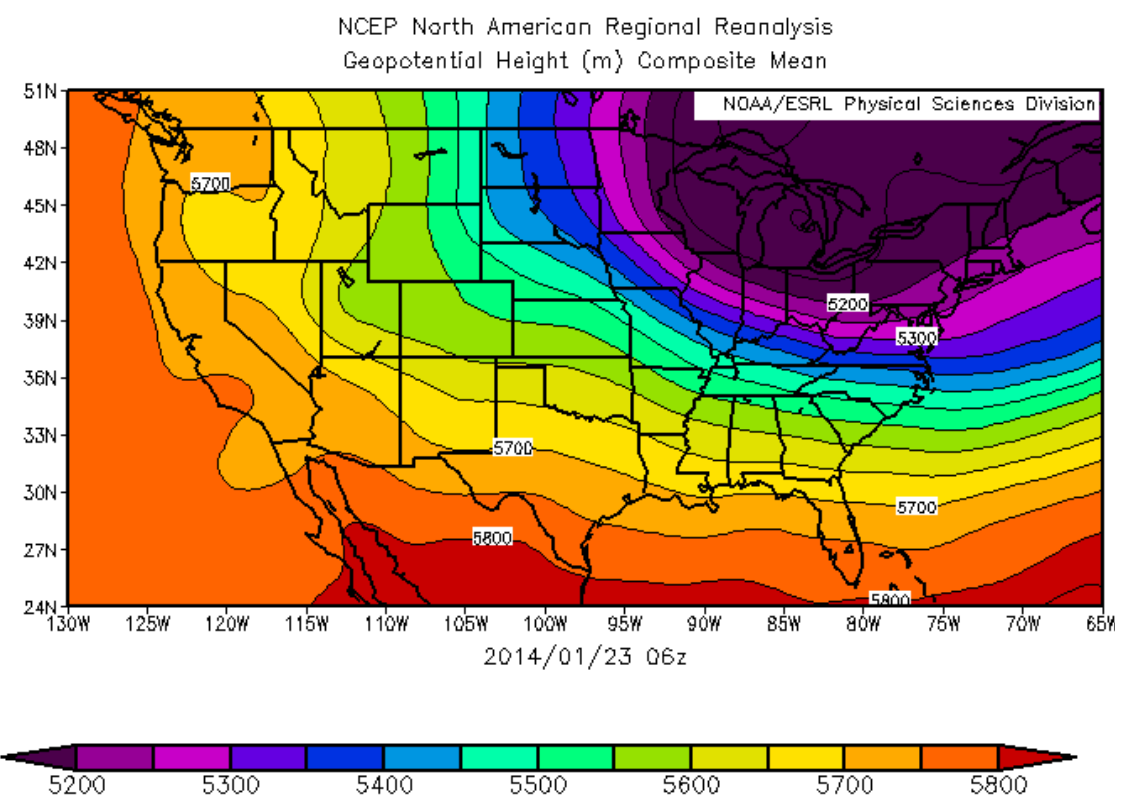


Figure A.2: 500mb Geopotential Height at 06Z 23 January 2014

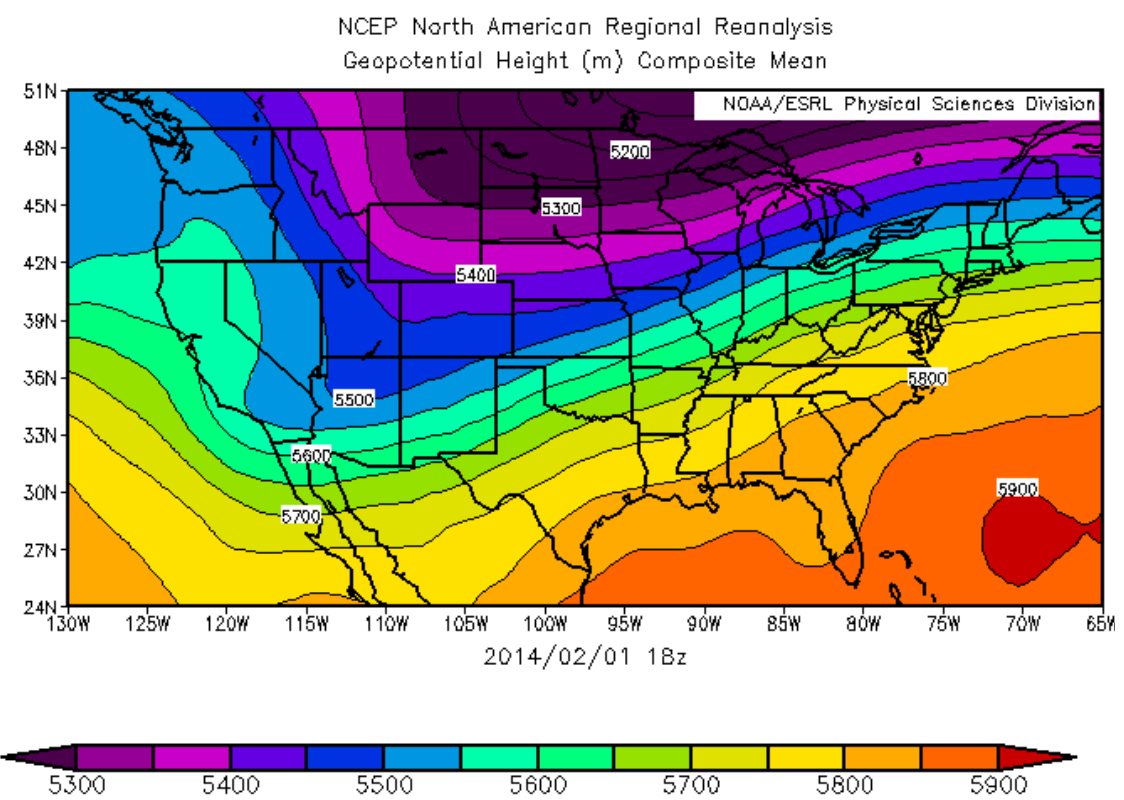


Figure A.3: 500mb Geopotential Height at 18Z 1 February 2014.

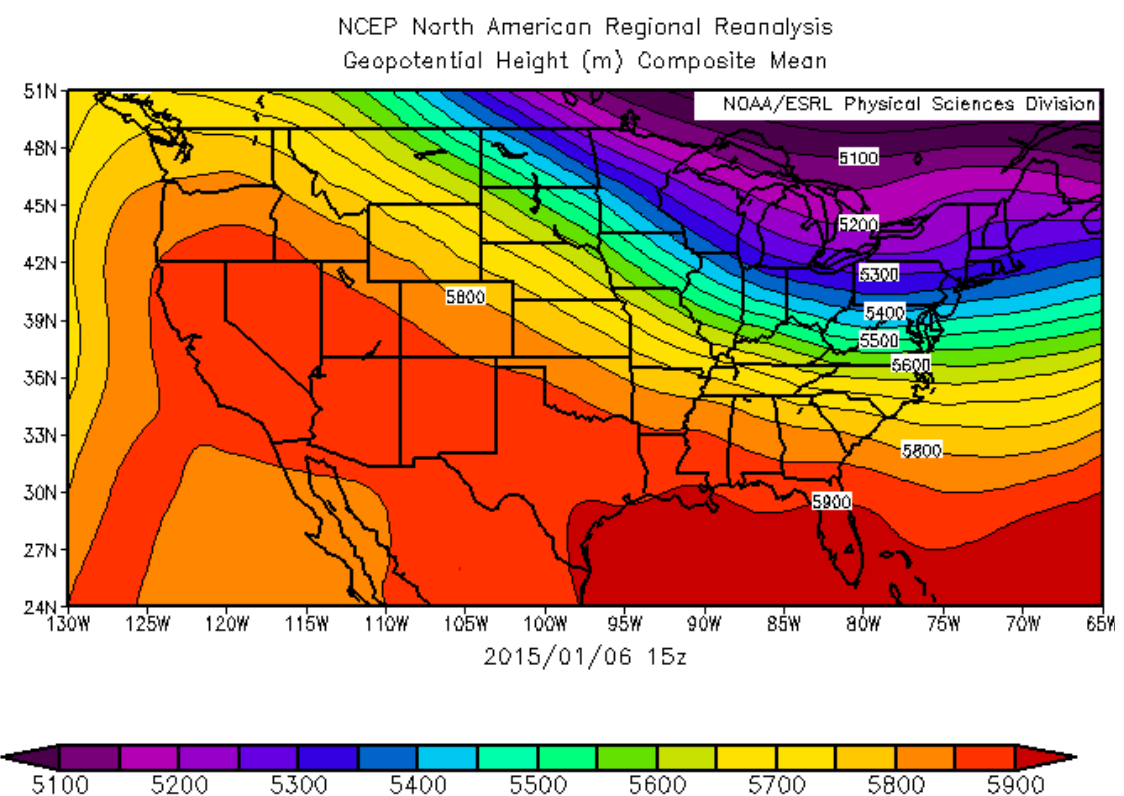


Figure A.4: 500mb Geopotential Height at 15Z 6 January 2015.

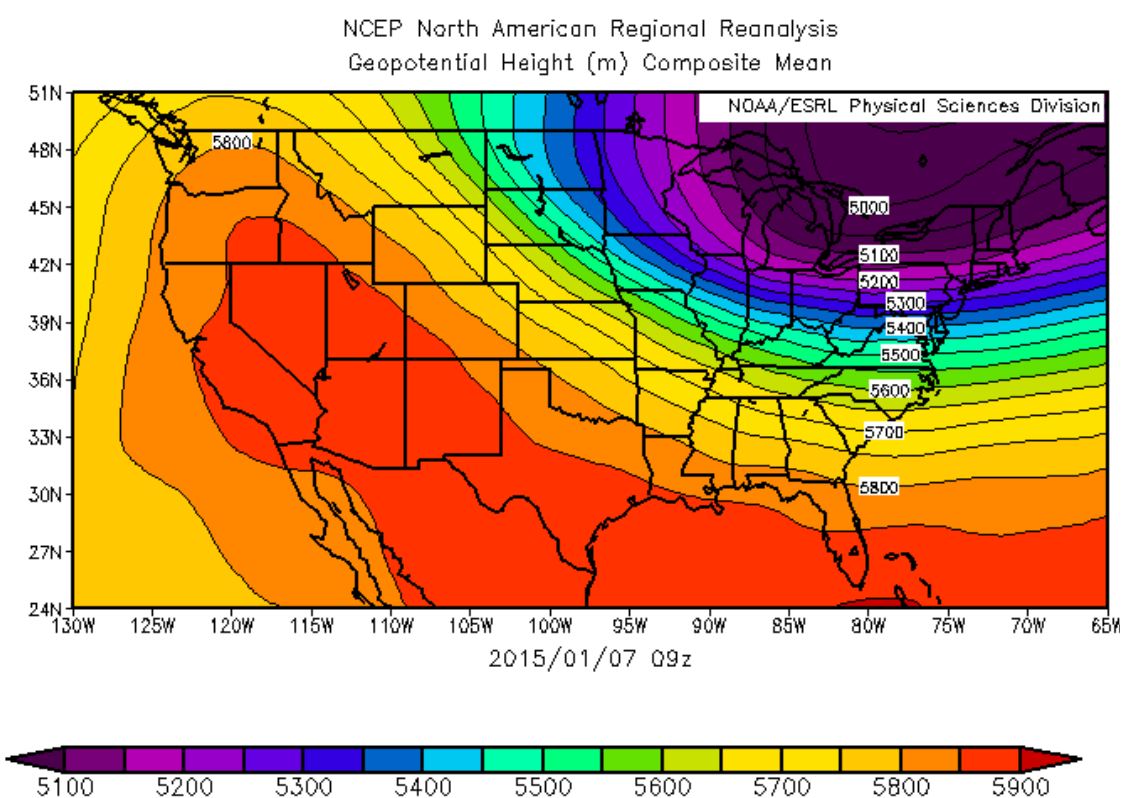


Figure A.5: 500mb Geopotential Height at 09Z 7 January 2015.

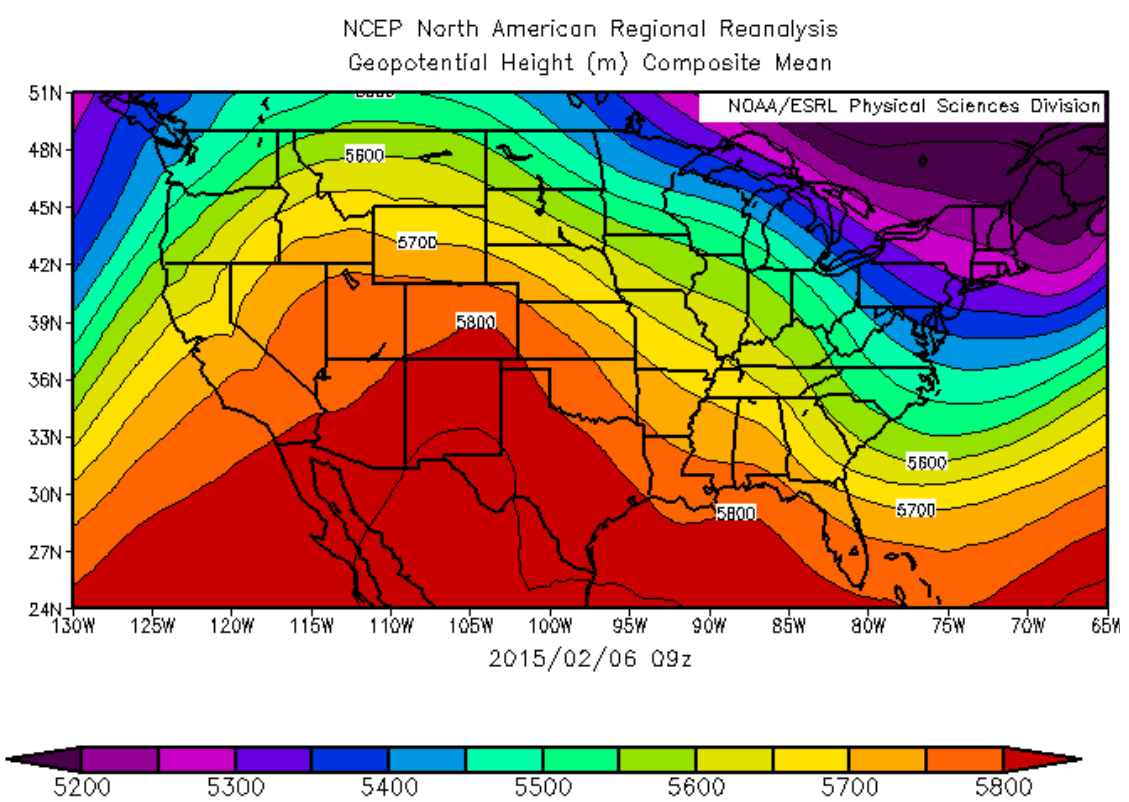


Figure A.6: 500mb Geopotential Height at 09Z 6 February 2015.

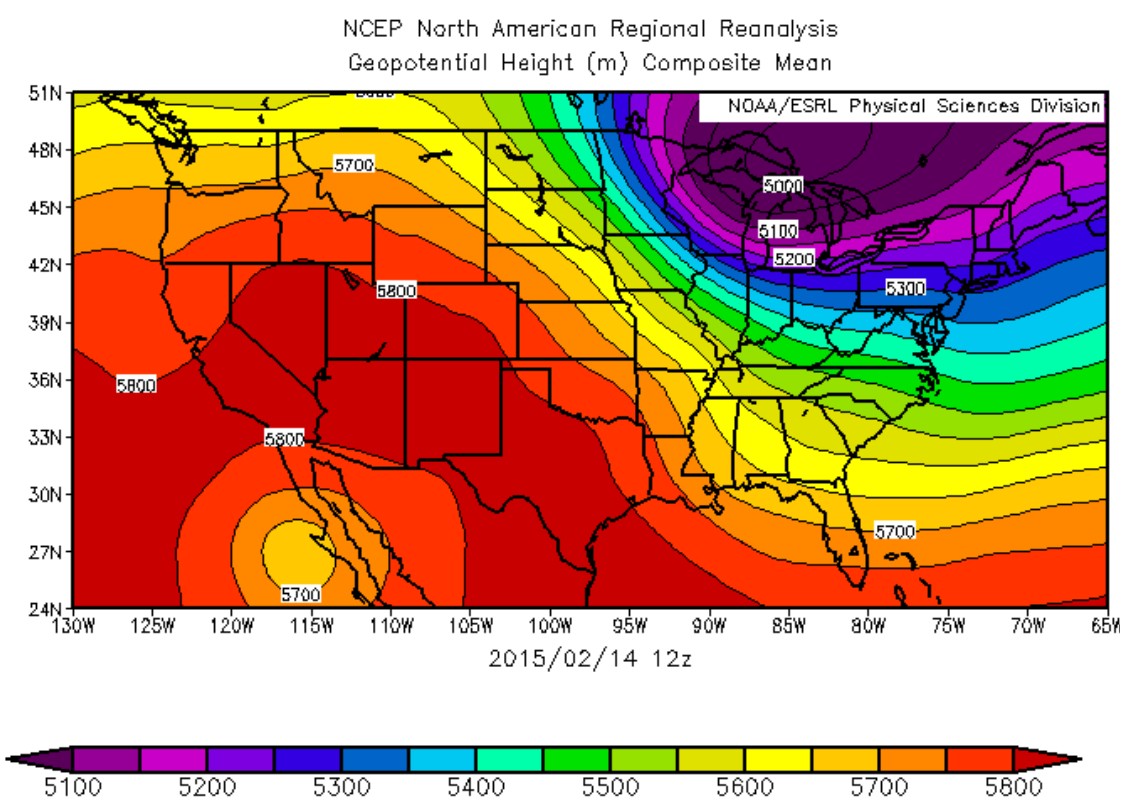


Figure A.7: 500mb Geopotential Height at 12Z 14 February 2015.

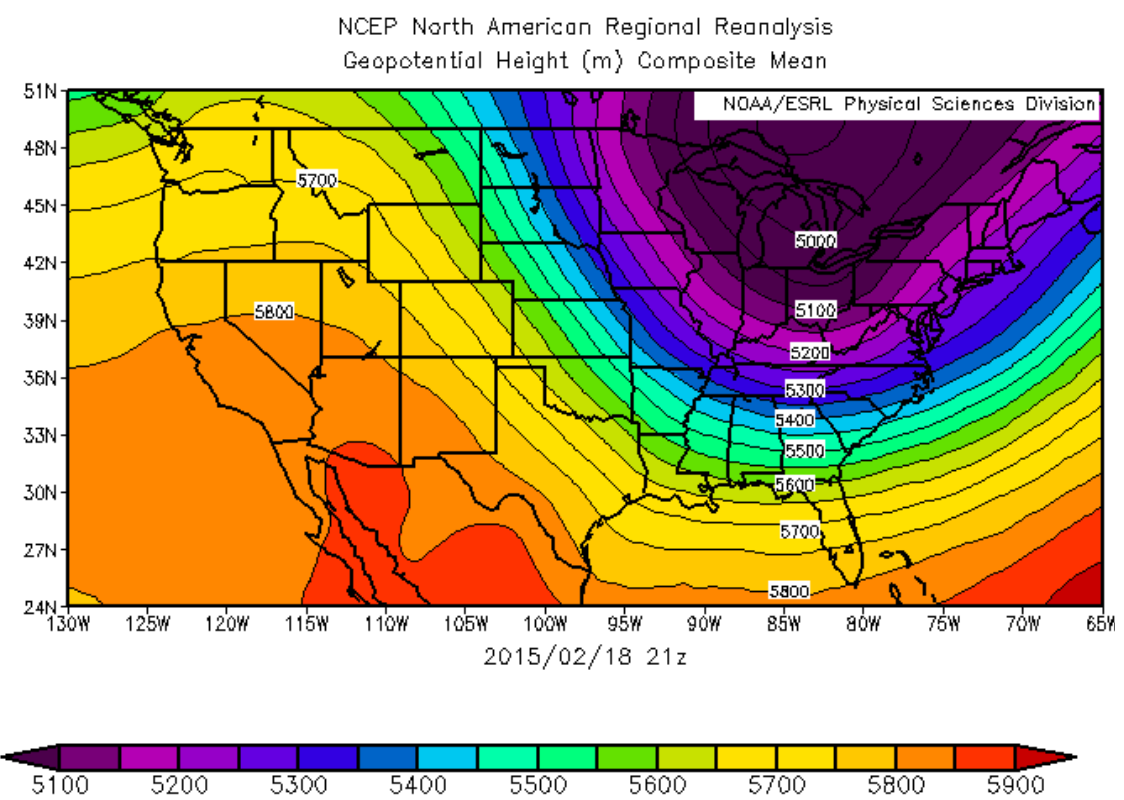


Figure A.8: 500mb Geopotential Height at 21Z 18 February 2015.

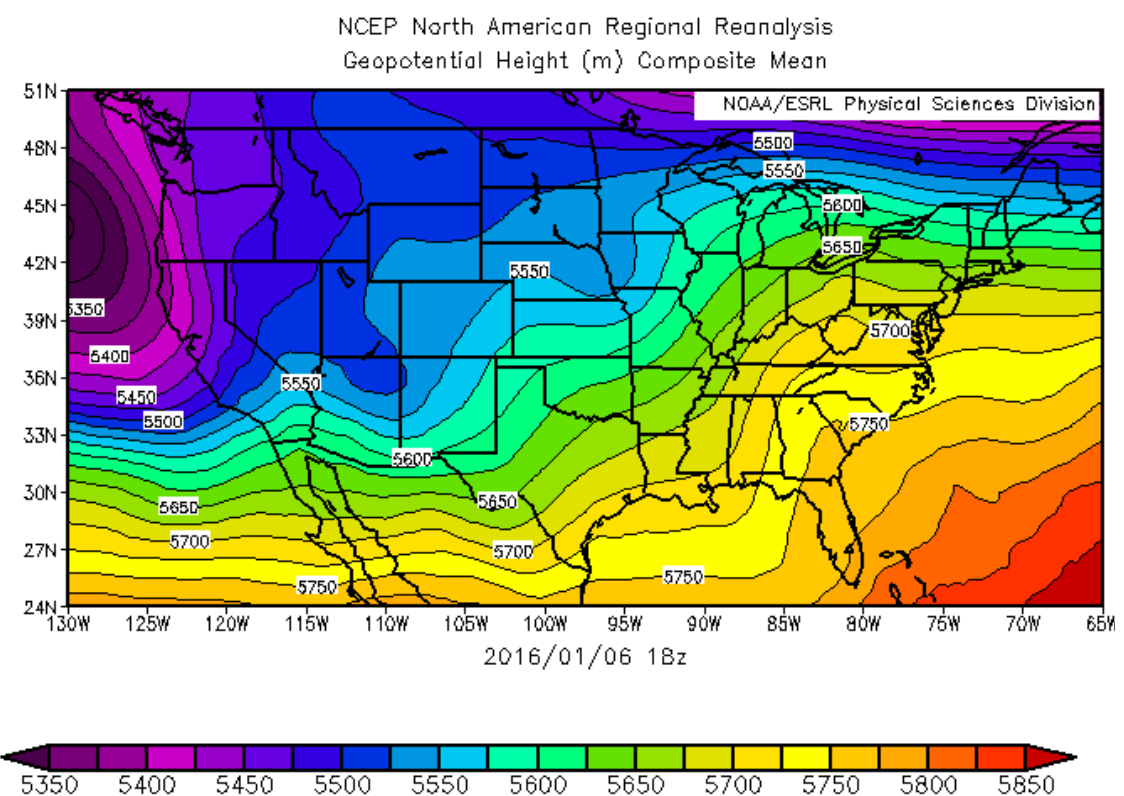


Figure A.9: 500mb Geopotential Height at 18Z 10 February 2016.

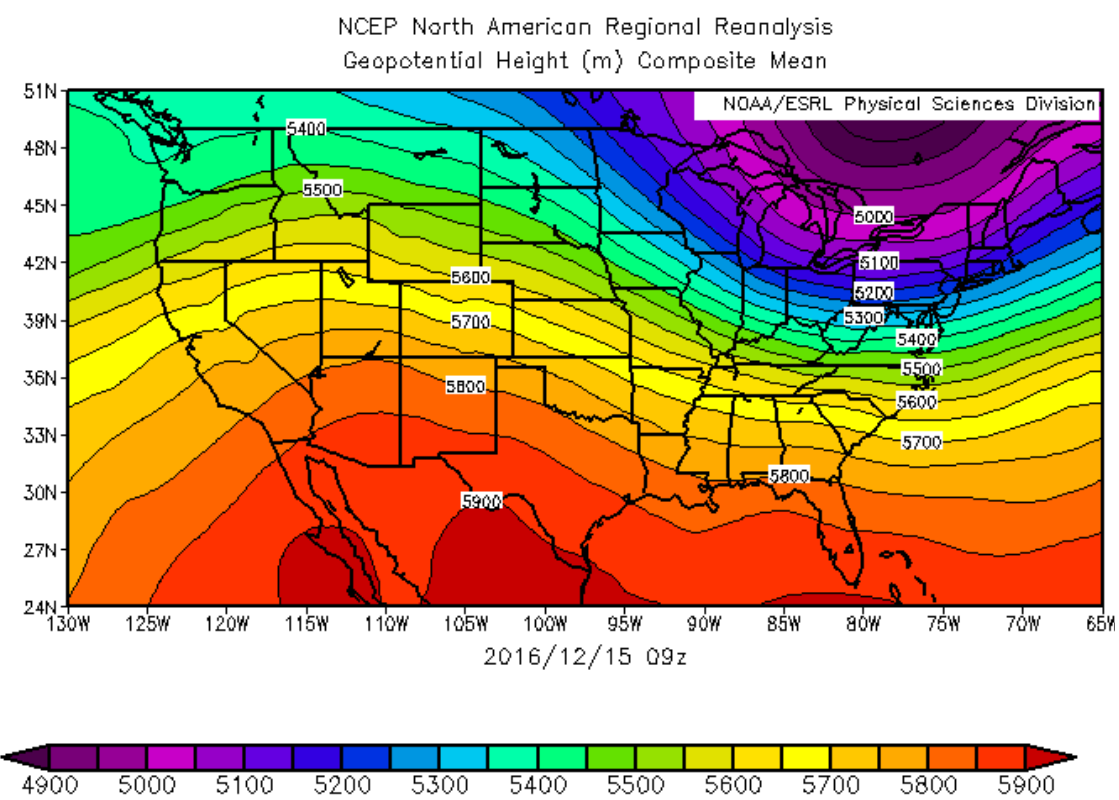


Figure A.10: 500mb Geopotential Height at 09Z 15 December 2016.

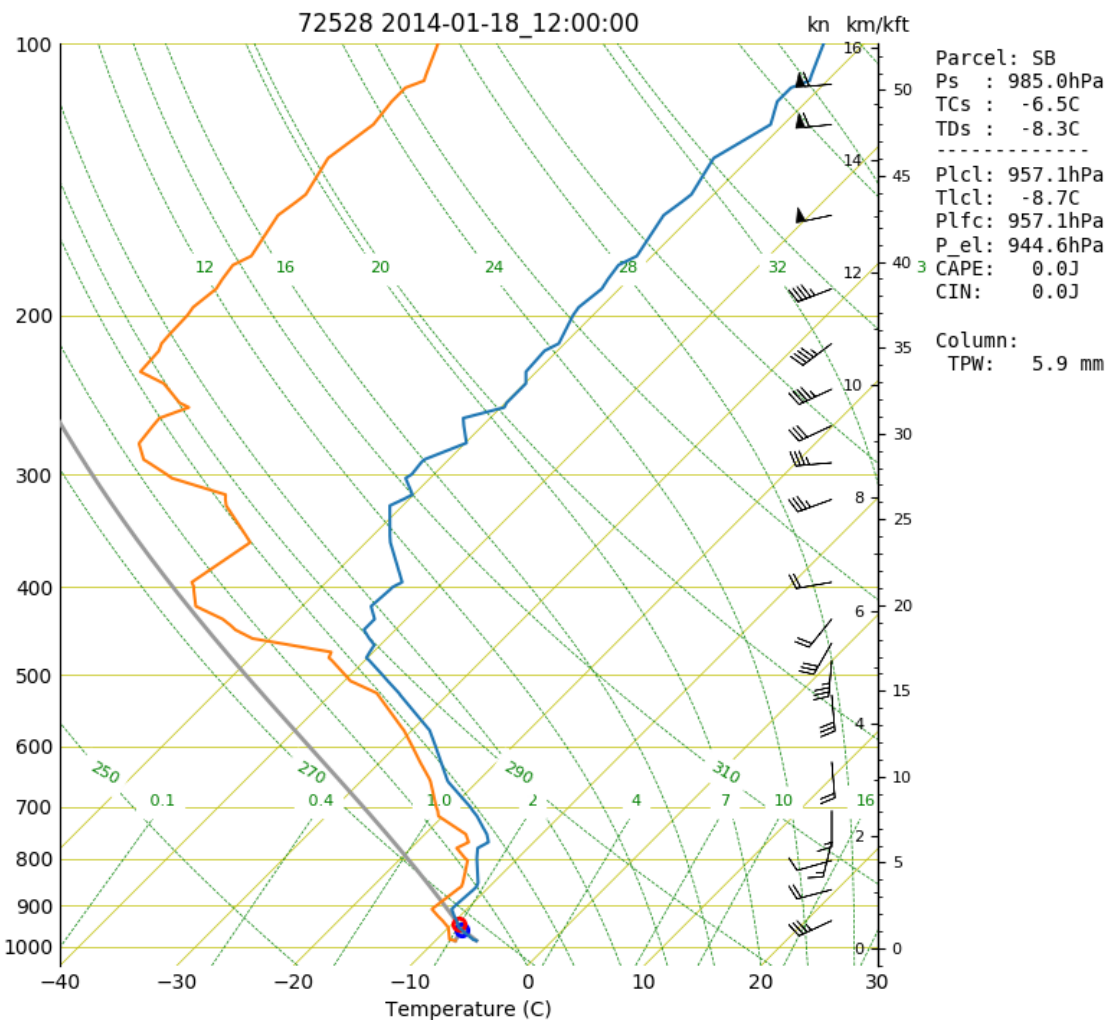


Figure A.11: SkewT/Log-P Chart from the BUF Radiosonde launched at 12Z 18

January 2014

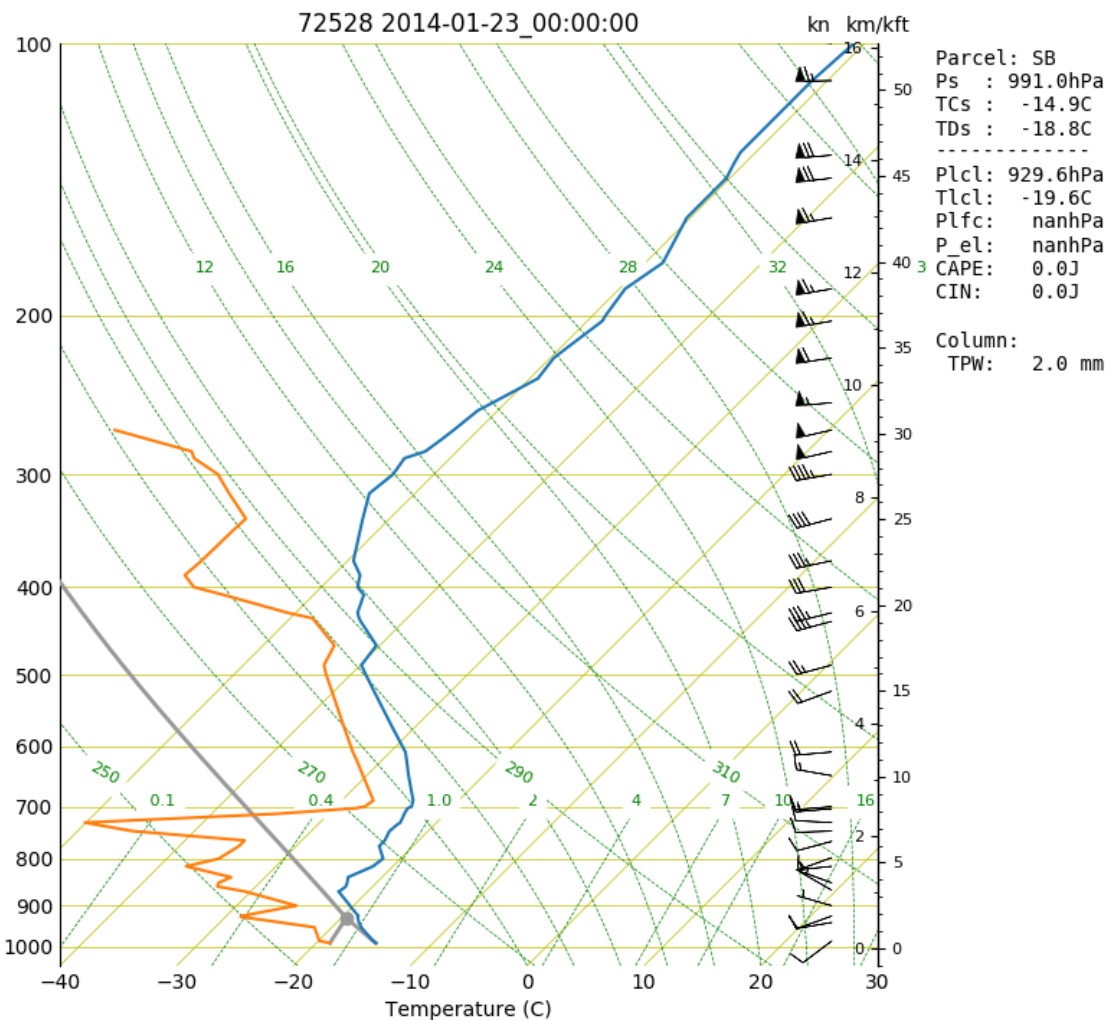


Figure A.12: SkewT/Log-P Chart from the BUF Radiosonde launched at 00Z 23 January 2014

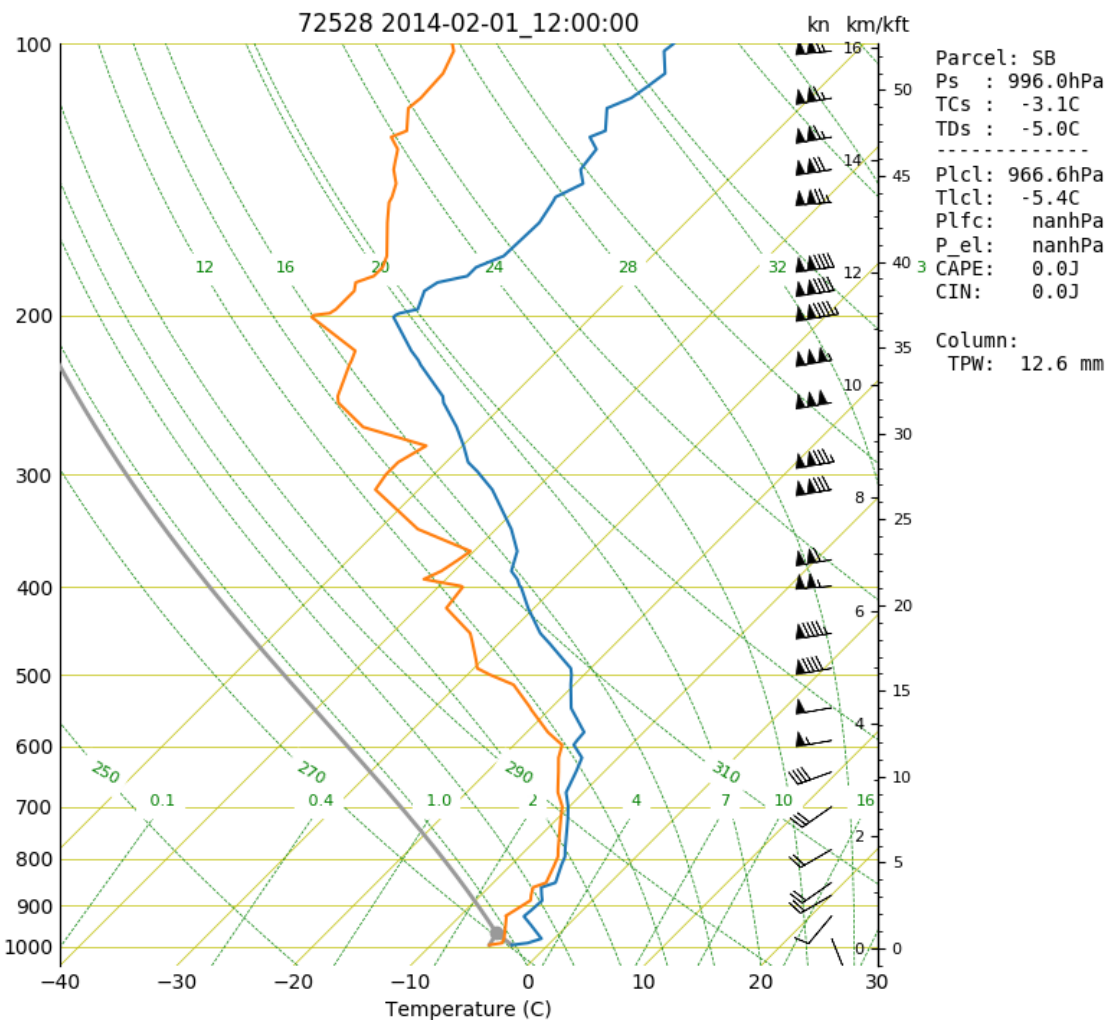


Figure A.13: SkewT/Log-P Chart from the BUF Radiosonde launched at 12Z 1

February 2014

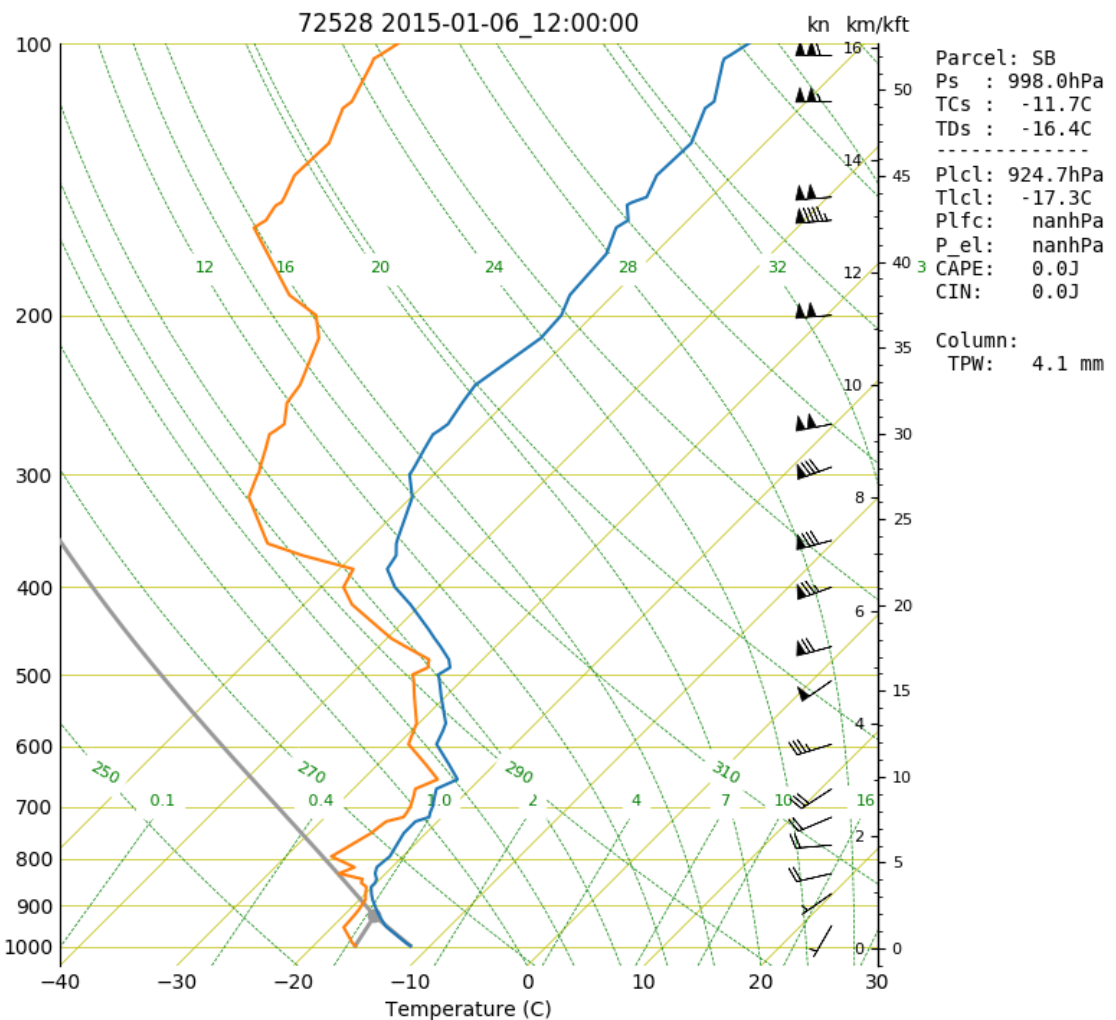


Figure A.14: SkewT/Log-P Chart from the BUF Radiosonde launched at 00Z 6

January 2015

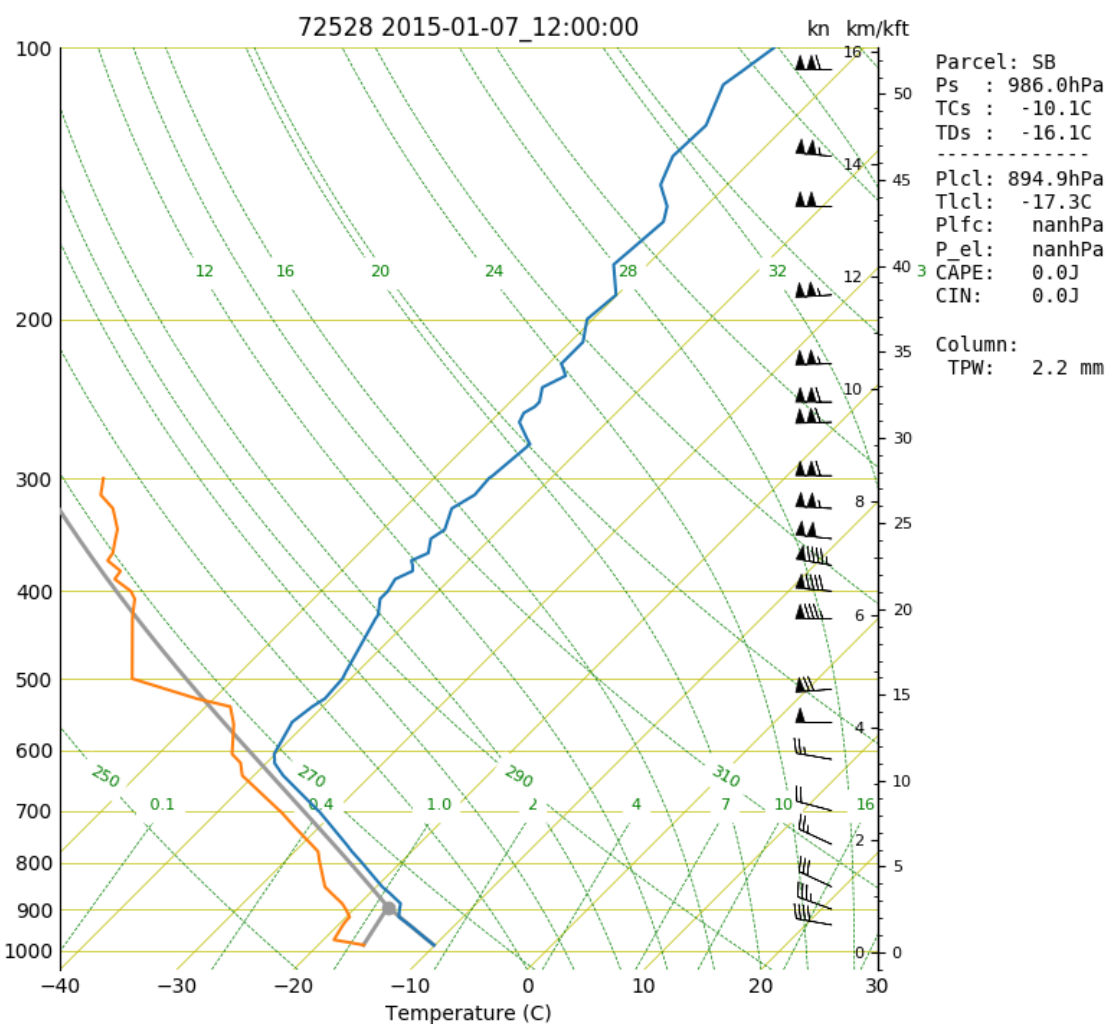


Figure A.15: SkewT/Log-P Chart from the BUF Radiosonde launched at 12Z 7

January 2015

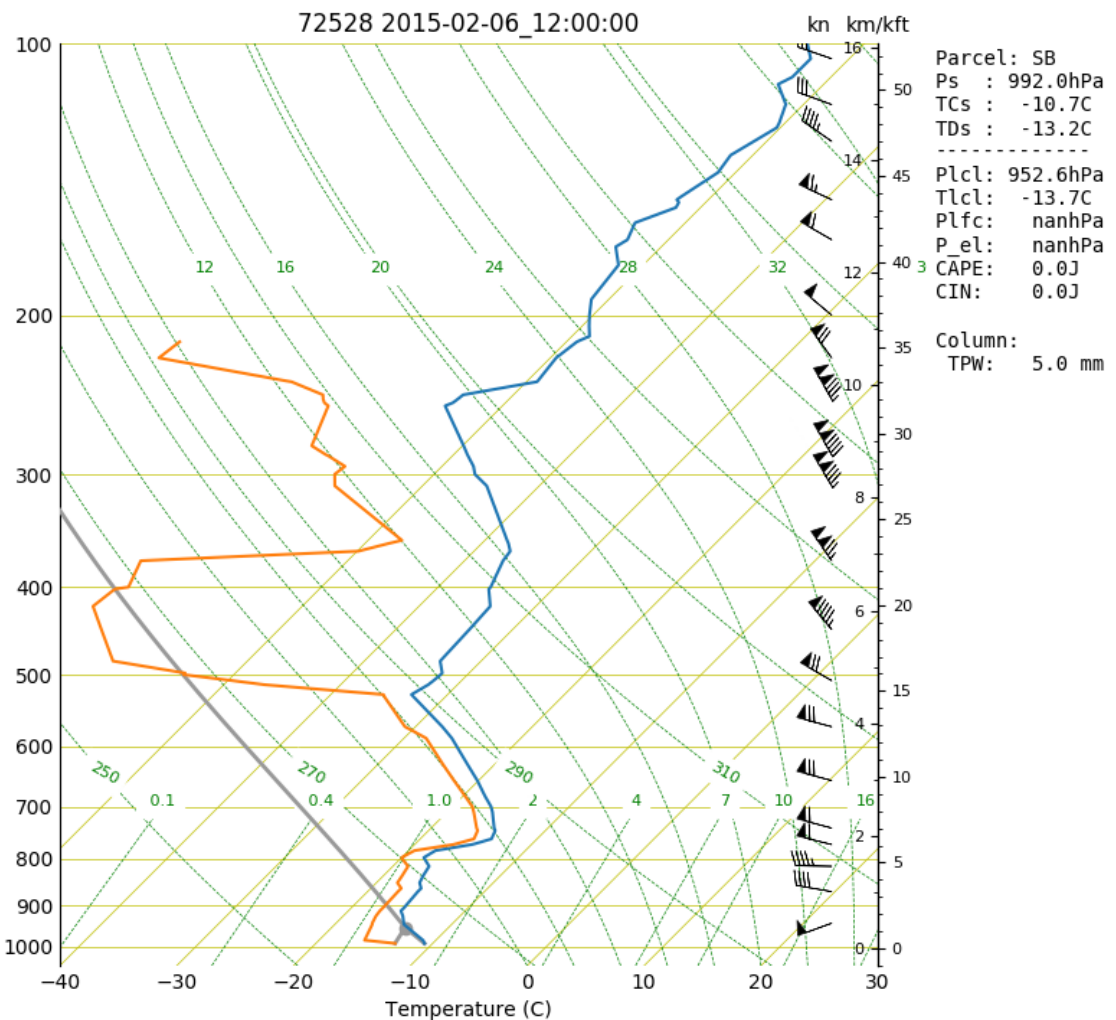


Figure A.16: SkewT/Log-P Chart from the BUF Radiosonde launched at 00Z 6

February 2015

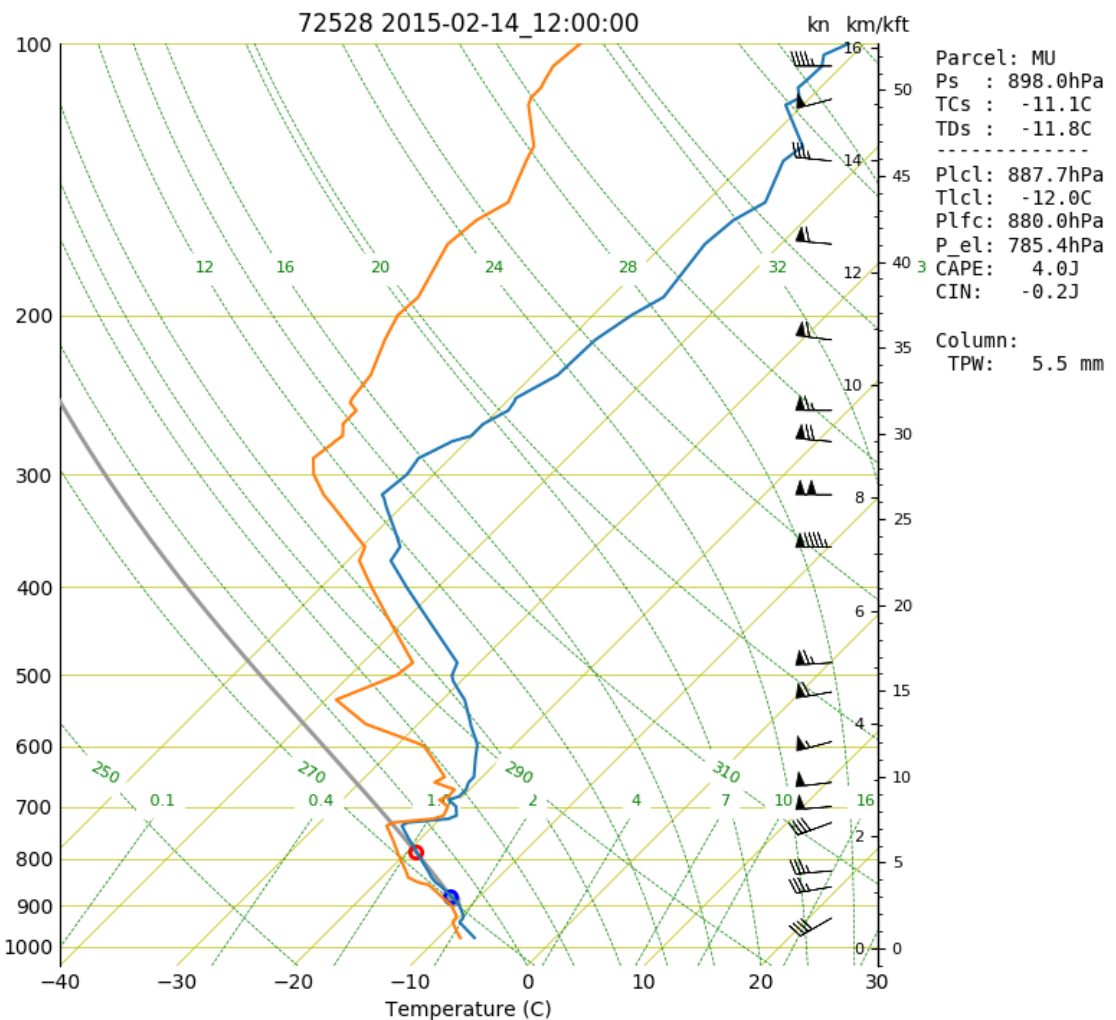
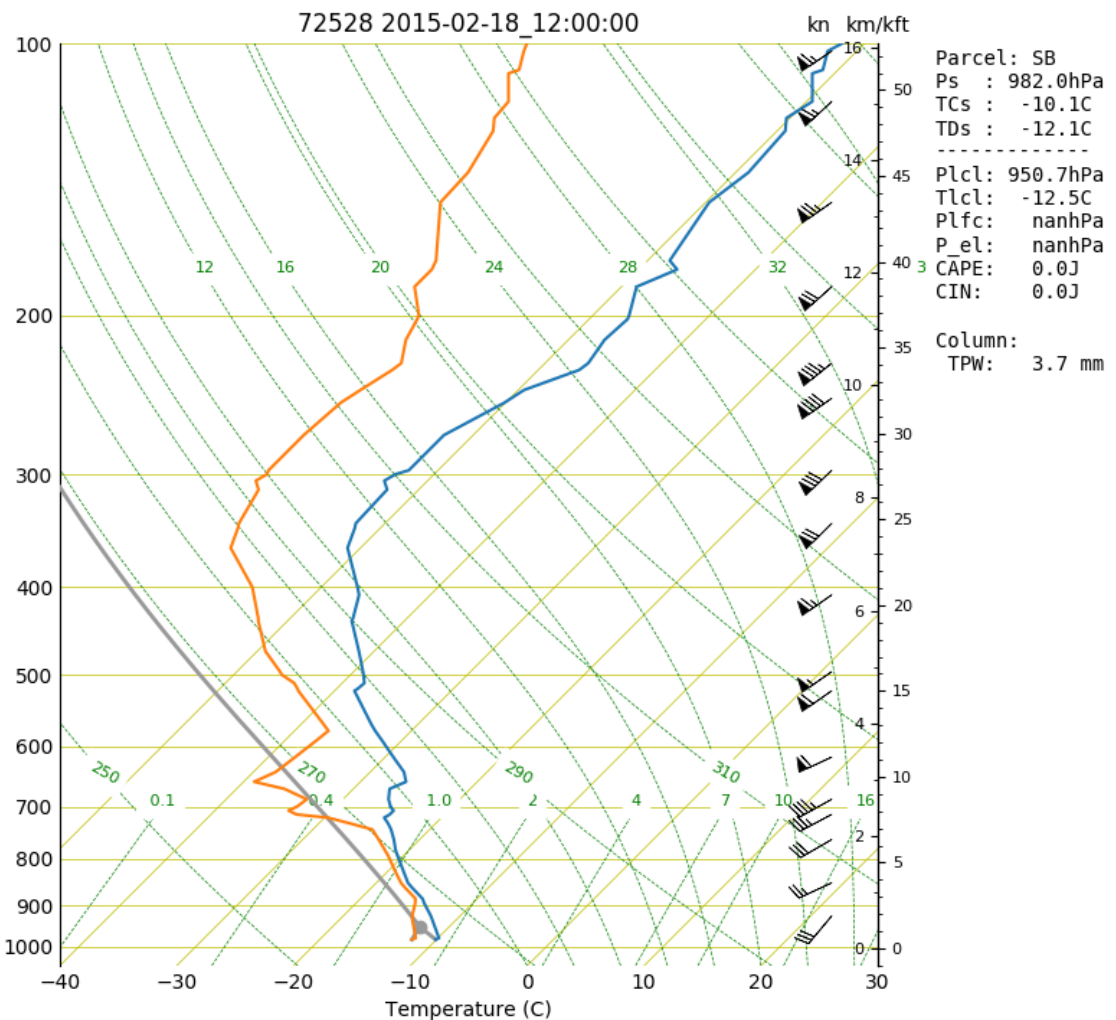


Figure A.17: SkewT/Log-P Chart from the BUF Radiosonde launched at 12Z 14

February 2015



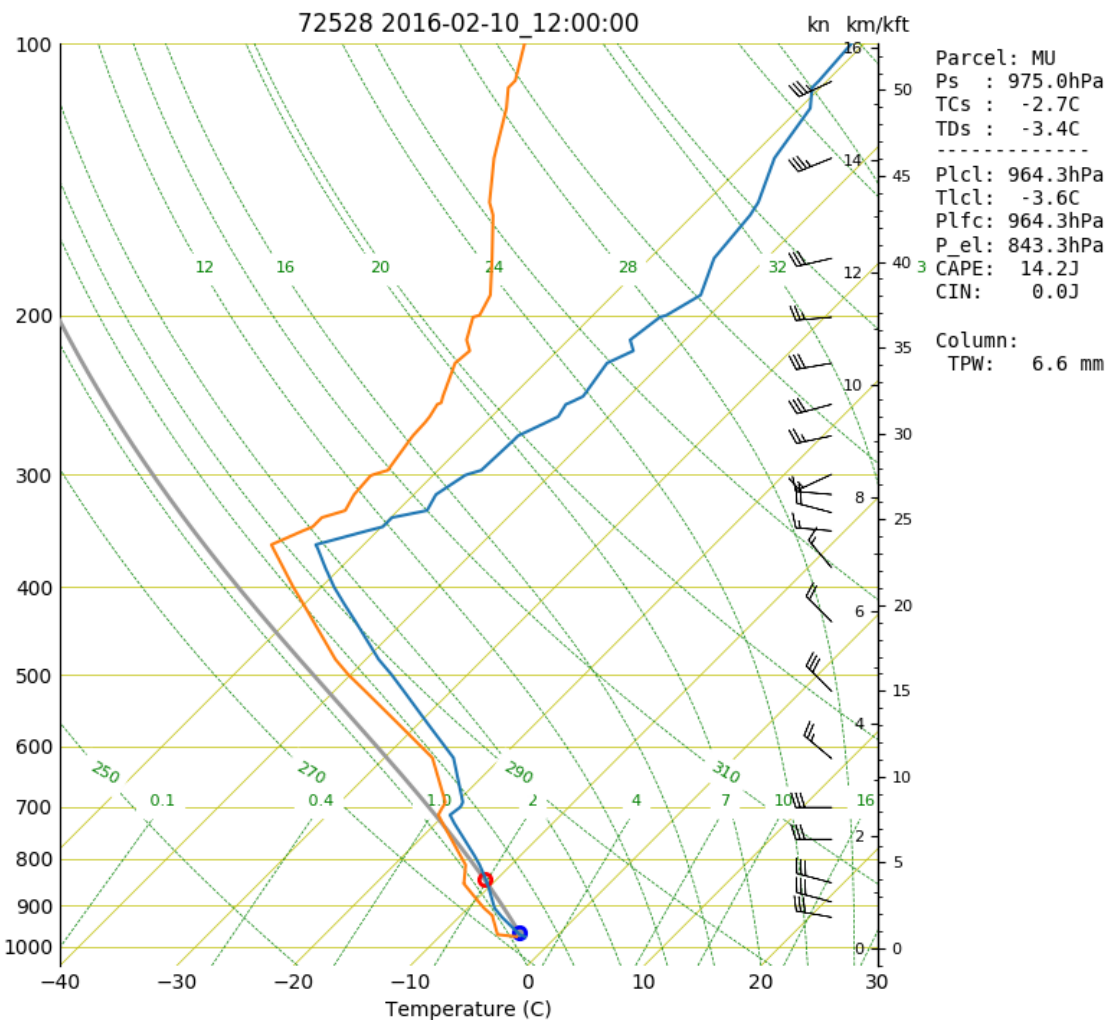


Figure A.19: SkewT/Log-P Chart from the BUF Radiosonde launched at 12Z 10

February 2016

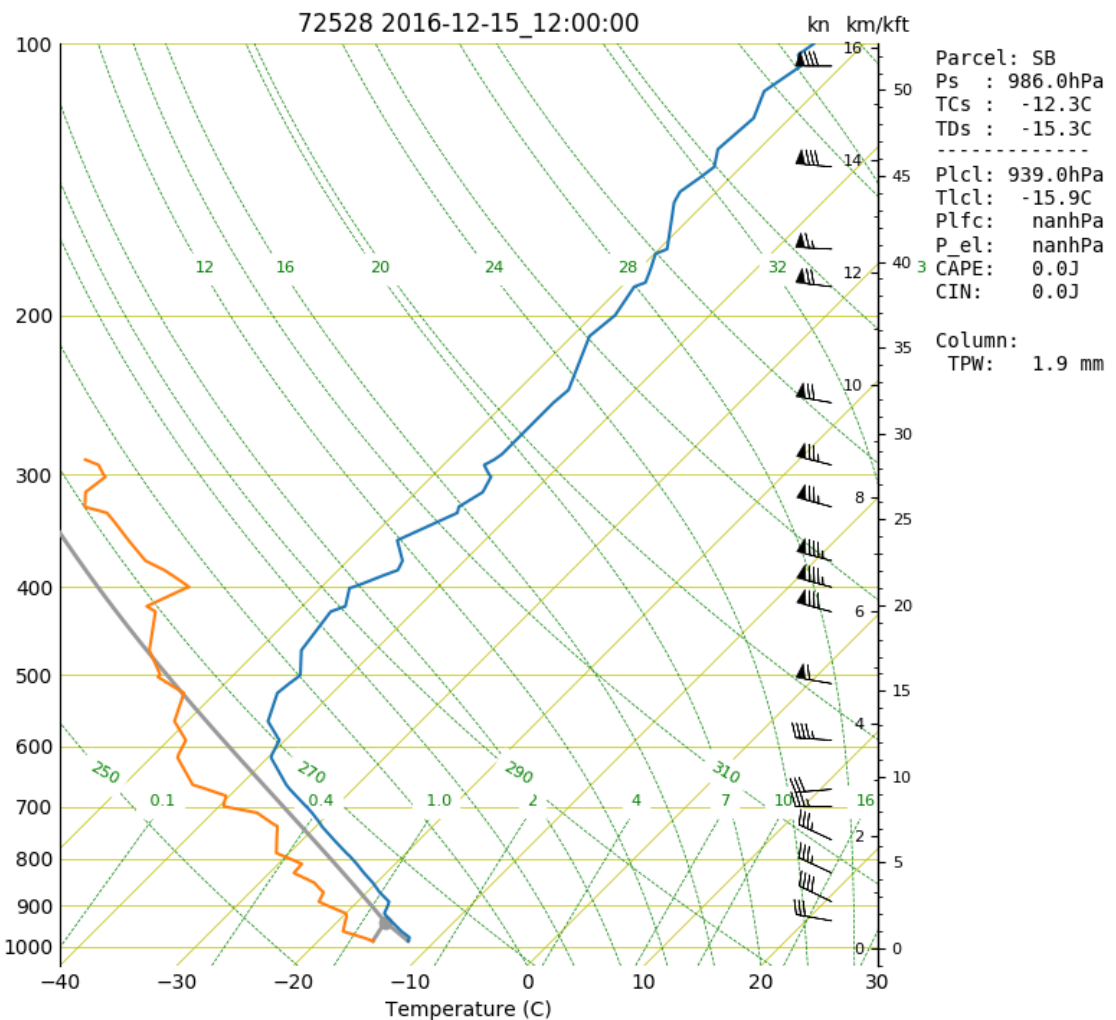


Figure A.20: SkewT/Log-P Chart from the BUF Radiosonde launched at 12Z 15

December 2016

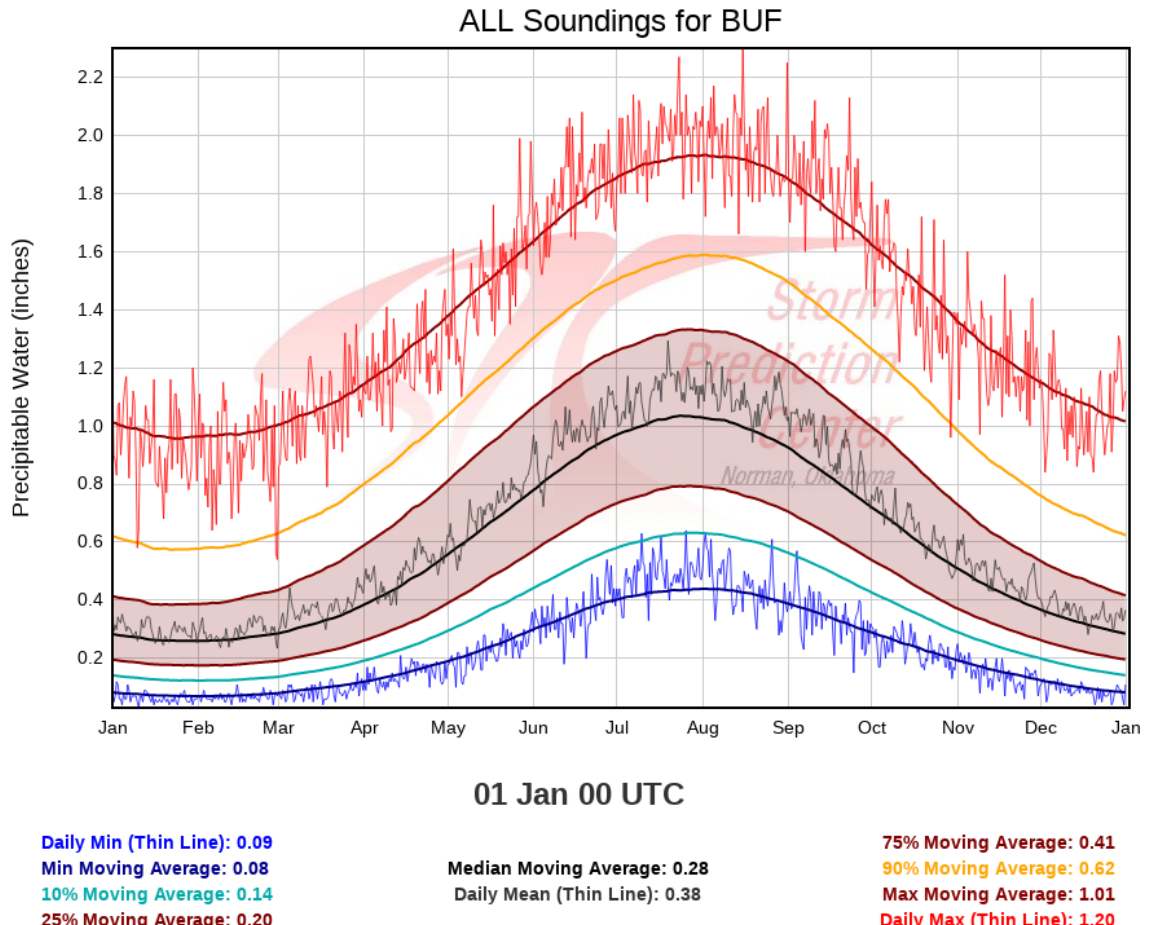


Figure A.21: Sounding Precipitable Water Climatology for BUF

## Bibliography

- Cunningham, J. G., W. D. Zittel, R. R. Lee, and R. L. Ice, 2013: Methods for Identifying Systematic Differential Reflectivity Biases on the Operational WSR-88D Network. *36th Conf. on Radar Meteorology*, Breckinridge, CO, Amer. Meteor. Soc., 9B.5, URL <https://ams.confex.com/ams/36Radar/webprogram/Paper228792.html>.
- Fabry, F., 2015: *Radar Meteorology: Principles and Practice*. Cambridge University Press, 256 pp.
- Hassan, D., P. A. Taylor, and G. A. Isaac, 2017: Snowfall Rate Estimation using C-Band Polarimetric Radars. *Meteor. Appl.*, **24** (1), 142–156, URL <http://doi.org/10.1002/met.1613>.
- Helmus, J. J. and S. M. Collis, 2016: The Python ARM Radar Toolkit (Py-ART), a Library for Working with Weather Radar Data in the Python Programming Language. *JORS*, **4** (1), e25, URL <http://doi.org/10.5334/jors.119>.
- Hubbert, J. and F. Pratte, 2006: Differential Reflectivity Calibration for NEXRAD. *2006 IEEE International Symposium on Geoscience and Remote Sensing*, 519–522, URL <https://doi.org/10.1109/IGARSS.2006.138>.
- Markovsky, I. and S. V. Huffel, 2007: Overview of total least-squares methods. *Elsevier BV*, URL <http://doi.org/10.1016/j.sigpro.2007.04.004>.
- Pauley, P. M. and X. Wu, 1990: The theoretical, discrete, and actual response of the Barnes objective analysis scheme for one- and two-dimensional fields. *Mon. Wea. Rev.*, **118** (5), 1145–1164, URL [http://doi.org/10.1175/1520-0493\(1990\)118<1145:TTDAAR>2.0.CO;2](http://doi.org/10.1175/1520-0493(1990)118<1145:TTDAAR>2.0.CO;2).
- Rogers, R. and M. Yau, 1989: *A Short Course in Cloud Physics*, Vol. 113. Elsevier, 290 pp.
- Silverman, B. W., 1986: *Density Estimation for Statistics and Data Analysis*, Vol. 26. Chapman and Hall, 176 pp.
- Torres, S. and C. Curtis, 2007: Initial Implementation of Super-Resolution Data on the NEXRAD Network. *23rd Conf. on IIPS*, San Antonio, TX, Amer. Meteor. Soc., 5B.10, URL [https://ams.confex.com/ams/87ANNUAL/techprogram/paper\\_116240.htm](https://ams.confex.com/ams/87ANNUAL/techprogram/paper_116240.htm).

Zittel, W. D., R. R. Lee, L. M. R. J. G. Cunningham, J. Schultz, and R. L. Ice, 2015: Geographical and Seasonal Availability of Light Rain, Dry Snow, and Bragg Scatter to Estimate WSR-88D  $z_{DR}$  System Bias. *31st Conf. on EIP*, Phoenix, AZ, Amer. Meteor. Soc., 11.2, URL <https://ams.confex.com/ams/95Annual/webprogram/Paper265374.html>.

Zrnic, D., V. M. Melnikov, and J. K. Carter, 2006: Calibrating Differential Reflectivity on the WSR-88D. *Journal of Atmospheric and Oceanic Technology*, **23** (7), 944–951, doi:10.1175/JTECH1893.1, URL <https://doi.org/10.1175/JTECH1893.1>.